



Review

Metal/Semiconductor Nanocomposites for Photocatalysis: Fundamentals, Structures, Applications and Properties

Yong-sheng Fu , Jun Li * and Jianguo Li

School of Materials Science and Engineering, Shanghai Jiao Tong University, Shanghai 200240, China; fuys648@163.com (Y.-s.F.); lijg@sjtu.edu.cn (J.L.)

* Correspondence: li.jun@sjtu.edu.cn; Tel.: +86-156-0189-7272

Received: 1 February 2019; Accepted: 19 February 2019; Published: 4 March 2019



Abstract: Due to the capability of utilizing light energy to drive chemical reactions, photocatalysis has been widely accepted as a green technology to help us address the increasingly severe environment and energy issues facing human society. To date, a large amount of research has been devoted to enhancing the properties of photocatalysts. As reported, coupling semiconductors with metals is one of the most effective methods to achieve high-performance photocatalysts. The excellent properties of metal/semiconductor (M/S) nanocomposite photocatalysts originate in two aspects: (a) improved charge separation at the metal-semiconductor interface; and (b) increased absorption of visible light due to the surface plasmon resonance of metals. So far, many M/S nanocomposite photocatalysts with different structures have been developed for the application in environmental remediation, selective organic transformation, hydrogen evolution, and disinfection. Herein, we will give a review on the M/S nanocomposite photocatalysts, regarding their fundamentals, structures (as well as their typical synthetic approaches), applications and properties. Finally, we will also present our perspective on the future development of M/S nanocomposite photocatalysts.

Keywords: nanocomposite photocatalyst; environmental remediation; selective organic transformation; hydrogen evolution; disinfection

1. Introduction

Since the discovery of water splitting on a TiO₂ electrode under irradiation of ultraviolet (UV) light by Fujishima and Honda in 1972, many semiconductors, such as CdS, ZnO, SrTiO₃ and g-C₃N₄, have been demonstrated to exhibit photocatalytic properties and, through the efforts of researchers, the application areas of semiconductor photocatalysts have been greatly extended [1–14]. Unfortunately, due to fast charge separation and limited light absorption, the properties of semiconductor photocatalysts are relatively unsatisfactory for practical application [15–17]. To improve the properties of semiconductor photocatalysts, several strategies have been proposed by researchers, such as doping, dye-sensitization, coupling, etc. [18–27]. However, each of these strategies has its own pros and cons. Toward the strategy of doping, the band structures of semiconductor photocatalysts could be modulated by the doping atoms to exhibit better properties for light absorption, but the doped semiconductor photocatalysts could be more susceptible to photo-corrosion and the charge recombination of the doped semiconductor photocatalysts could be aggravated at the defects introduced by the doping atoms [19,21,27]. As for the strategy of dye-sensitization, although the light-sensitive dyes can absorb light more efficiently and transfer the photoexcited electrons to the semiconductor photocatalysts, the light-sensitive dyes are susceptible to chemical corrosion, resulting in the poor stability of dye-sensitized semiconductor photocatalysts [24–26]. Coupling, as a strategy

with a relatively short history, has aroused great interest among researchers since its very beginning. When coupled with metals, especially the noble metals, the properties of semiconductor photocatalysts can be considerably improved due to the enhanced charge separation at the metal–semiconductor interface and the enhanced visible light absorption caused by the surface plasmon resonance (SPR) of metals [28–30]. Except for the high cost of noble metals, the main drawback of the coupling strategy used to be the poor control of the process of coupling semiconductors with metals. However, with the development of nanotechnology, the coupling process now could be delicately controlled and several new structures have been synthesized to improve the properties of metal/semiconductor (M/S) nanocomposite photocatalysts [29,31].

Herein, we would like to review the M/S nanocomposite photocatalysts regarding their fundamentals, structures (as well as their typical synthetic approaches), applications and properties. Finally, we will also present our perspective on the future development of M/S nanocomposite photocatalysts.

2. Fundamentals

2.1. Principles of Photocatalysis

As defined by the International Union of Pure and Applied Chemistry (IUPAC), photocatalysis is “A catalytic reaction involving light absorption by substrate” [32]. When semiconductor photocatalysts are irradiated by light with the photon energy larger than their band gap (BG) energy, the electrons in the valence band (VB) will be excited into the conduction band (CB), leaving positive holes in the VB. Because photocatalytic reactions are reactions happening at the surface of photocatalysts, the photo-induced free charge carriers need first to diffuse into the active sites on the surface of photocatalysts before they can induce photocatalytic reactions [33–35]. The photocatalytic process is schematically presented in Figure 1. However, for a particular substrate, whether it can undergo chemical reactions on the semiconductor photocatalysts depends on the relative positions between its redox potentials and the band edges of semiconductor photocatalysts [36–38]. There are four possibilities as follows:

- (1) If the redox potential of the substrate is lower than the CB edge of the semiconductor photocatalyst, then the substrate can undergo reductive reactions.
- (2) If the redox potential of the substrate is higher than the VB edge of the semiconductor photocatalyst, then the substrate can undergo oxidative reactions.
- (3) If the redox potential of the substrate is higher than the CB edge or lower than the VB of the semiconductor photocatalyst, then the substrate can undergo neither reductive nor oxidative reactions.
- (4) If the redox potential of the substrate is lower than the CB edge and higher than the VB of the semiconductor photocatalyst, then the substrate can undergo either reductive or oxidative reactions.

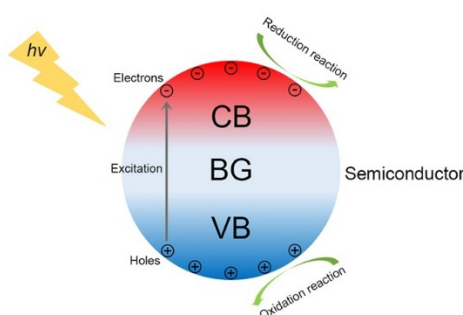


Figure 1. Schematic diagram for the photocatalytic process.

2.2. Mechanisms for the Enhanced Properties of Metal/Semiconductor (M/S) Nanocomposite Photocatalysts

As mentioned above, by coupling with different metals, the mechanisms for the enhanced properties of M/S nanocomposite photocatalysts can be divided into two categories, i.e., the enhanced charge separation at the metal–semiconductor interface and the enhanced visible light absorption due to the SPR of metals.

2.2.1. Enhanced Charge Separation

The enhanced charge separation of M/S nanocomposite photocatalysts originates from the electron transfer across the metal–semiconductor interface [31,39–41]. When a semiconductor is coupled with a metal, which possesses a higher work function than that of the semiconductor (it is the most common case for M/S nanocomposite photocatalysts), then the electrons will flow from the semiconductor to the metal until their Fermi levels (i.e., $E_{F,m}$ and $E_{F,s}$) are aligned, leading to the upward bending of the band edges in the semiconductor as revealed in Figure 2. Accompanied with the band bending, a Schottky barrier (i.e., ϕ_{SB} in Figure 2) forms at the metal–semiconductor interface [39]. As has been shown, the efficiency of electron transfer across the metal–semiconductor interface increases with the height of the Schottky barrier [42]. In addition, the metals in M/S nanocomposite photocatalysts not only act as the electron reservoir to enhance the charge separation of the semiconductors, but also provide active sites for reductive reactions, hence dramatically improving the properties of M/S nanocomposite photocatalysts [43].

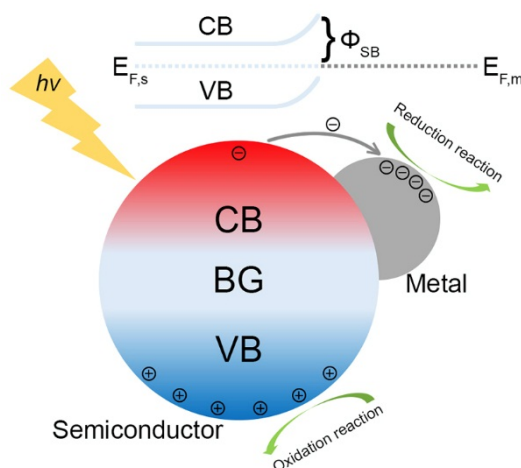


Figure 2. Enhanced charge separation at the metal–semiconductor interface.

2.2.2. Enhanced Visible Light Absorption

When coupled with metals such as Ag and Au, the SPR of metals could endow the M/S nanocomposite photocatalysts with enhanced absorption toward visible light [44,45]. However, the mechanism governing the SPR-enhanced visible light absorption of M/S nanocomposite photocatalysts is still unclear [28,29,46,47]. So far, there exist three non-mutually exclusive mechanisms for the explanation of the SPR-enhanced properties of M/S nanocomposite photocatalysts under visible light irradiation, i.e., (a) SPR-induced electron injection from metals to semiconductors; (b) charge separation induced by near-field electric field (NFEF); (c) scattering-enhanced light absorption.

Surface Plasmon Resonance (SPR)-Induced Electron Injection

Due to the SPR of metals such as Au and Ag, the energy of excited electrons in the metals can be excited to the range between 1.0 and 4.0 eV above their Fermi levels. Then, the energetic electrons will overcome the Schottky barrier at the metal–semiconductor interface and transfer to the CB of semiconductors, leaving energetic holes in the metals, as schematically shown in Figure 3a. Thus, the

hot electrons in the semiconductors will drive reduction reactions and the hot holes in the metals will drive oxidation reactions.

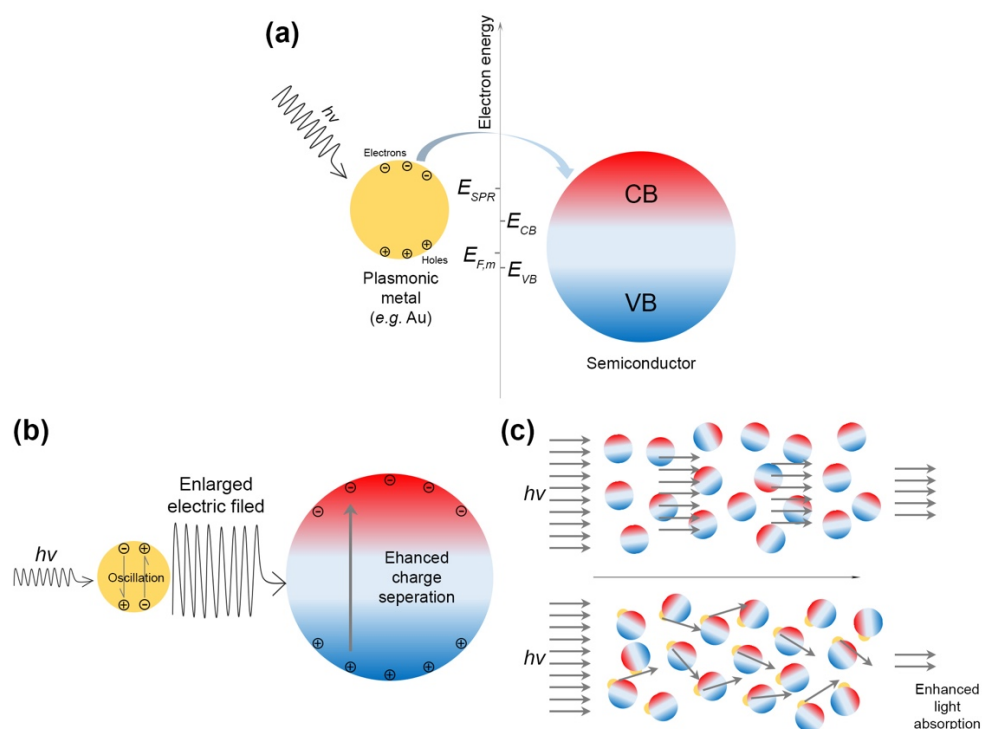


Figure 3. (a) SPR-induced electron injection; (b) Charge separation induced by NFEF; (c) Scattering-enhanced light absorption.

Charge Separation Induced by Near-Field Electric Field (NFEF)

Under visible light irradiation, the SPR-excited hot electrons in the metal particles of M/S nanocomposite photocatalysts will generate intense electric field in their proximity (i.e., NFEF), which could be up to 100–10000 times larger than the electric field of incident light. Since the formation rate of electron-hole pairs in the semiconductors of M/S nanocomposite photocatalysts is proportional to the intensity of the NFEF (more specifically, $|E|^2$), the generation of electron-hole pairs in M/S nanocomposite photocatalysts can be significantly enhanced. The process of NFEF-induced charge separation is schematically shown in Figure 3b.

Scattering-Enhanced Light Absorption

If the size of the metal particles in M/S nanocomposite photocatalysts is larger than 50 nm, the SPR-excited metal particles can efficiently scatter the incident light, leading to the increase of the path length of light through the M/S nanocomposite photocatalysts. Thus, the light absorption of M/S nanocomposite photocatalysts will be improved due to the increased path length of light, resulting in the enhancement of the properties of M/S nanocomposite photocatalysts. Figure 3c schematically reveals the scattering-enhanced photon absorption mechanism.

3. Structures of M/S Nanocomposite Photocatalysts

Based on the morphologies and synthetic approaches, the structures of M/S nanocomposite photocatalysts could be divided into six categories, i.e., the conventional structure, core-shell structure, yolk-shell structure, Janus structure, array structure and multi-junction structure, which are schematically shown in Figure 4.

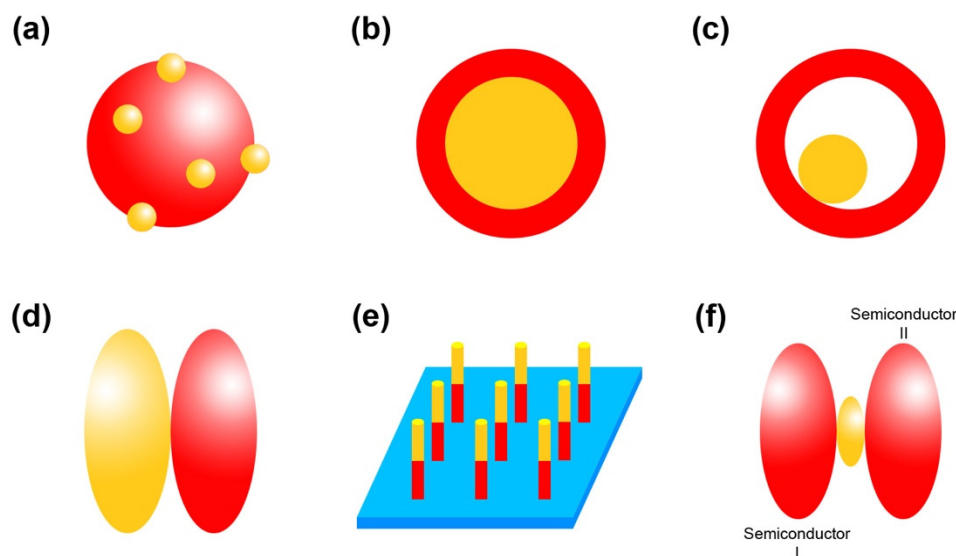


Figure 4. (a) Conventional structure; (b) Core-shell structure; (c) Yolk-shell structure; (d) Janus structure; (e) Array structure; (f) Multi-junction structure.

3.1. Conventional Structure

The conventional structure of M/S nanocomposite photocatalysts refers to the structure, in which the combination of semiconductor nanoparticles and metal nanoparticles is not delicately controlled. So far, many approaches have been developed to synthesize M/S nanocomposite photocatalysts with conventional structure, which include photoreduction, impregnation, deposition-precipitation, chemical vapor deposition (CVD) etc. [48–51].

3.1.1. Photoreduction

Since some chemical compounds containing metal element can be reduced to metal under irradiation, photoreduction is regarded as a facile approach to decorate semiconductor nanostructures with noble metal. Typically, in the work of Yu et al., hydrothermally-synthesized TiO₂ nanosheets were added to an aqueous solution of H₂PtCl₆. Under stirring and the irradiation of ultraviolet (UV) light, H₂PtCl₆ was reduced to Pt and deposited on TiO₂ nanosheets, leading to the formation of Pt-decorated TiO₂ nanosheets [48].

3.1.2. Impregnation

During the impregnation process, the combination of noble metal and semiconductor nanostructures is achieved through the attachment of noble metal precursor onto semiconductor substrate due to the van der Waals force, coulomb force or some other interactions between them. Typically, in the work of Lin et al., H₂PtCl₆ was added into a suspension of TiO₂ (B) nanofibers. Then the solvent was evaporated under stirring. Then, the as-obtained powders were heated in a reducing atmosphere to reduce H₂PtCl₆ absorbed on TiO₂ (B) nanofibers, leading to the formation of Pt-decorated TiO₂ (B) nanofibers [49].

3.1.3. Deposition-Precipitation

Deposition-precipitation is also a facile approach to synthesize M/S nanocomposites. Typically, in the work of Wu et al., TiO₂ nanoparticles were dispersed in an aqueous solution of chloroauric acid. Then NaOH solution was added into the suspension to adjust the pH value to the desired level. After stirring, the precipitates were filtered, washed and dried. Then, the as-obtained products were calcined to form the Au-decorated TiO₂ nanoparticles [50].

3.1.4. Chemical Vapor Deposition (CVD)

As is well known, CVD is a powerful approach in synthesizing nanostructure and is often utilized to prepare metal-decorated nanostructures. Typically, in the work of Shi et al., HAuCl_4 was vaporized at a high temperature in a tube furnace. Then, the vapor was blown at the TiO_2 nanorod arrays at a relatively low temperature with the carrier gas of nitrogen. Thus, the gold would deposit on the TiO_2 nanorods, leading to the formation of Au-decorated TiO_2 nanorod arrays [51].

3.2. Core-Shell Structure

The core-shell structure was first developed to improve the quantum yield of quantum dots in the 1990s [52]. After that, the core-shell structure attracted great interest from researchers and its application areas were greatly extended. In photocatalysis, M/S nanocomposite photocatalysts with core-shell structure occupy an important position due to their outstanding photocatalytic properties [53]. Besides, the enhanced charge transfer between metal and semiconductor, the core-shell structure can also hinder the aggregation of particles and protect the metal core from undesired corrosion or dissolution during the photocatalytic process.

The synthesis of core-shell M/S nanoparticles usually involves the coating of a semiconductor layer on metal nanoparticles. For example, in the work of Sudeep, photocatalytic Ag@TiO_2 core-shell nanoparticles were synthesized through controlled hydrolysis of titanium-(triethanolaminate) isopropoxide (TTEAIP) on the surface of Ag nanoparticles. Briefly, TTEAIP and silver nitrate were added into 2-propanol followed by stirring. Then dimethyl formamide (DMF) was added to the solution. Next, the solution was heated and refluxed. During this process, silver nitrate was first reduced to Ag nanoparticles by DMF. Then, due to the interaction between Ag nanoparticles and triethanolamine ligands, TTEAIP hydrolyzed on the surface of Ag nanoparticles, leading to the formation of Ag@TiO_2 core-shell nanoparticles [54].

3.3. Yolk-Shell Structure

The yolk-shell structure originates from the pioneer work of Xia's group as a variation of the core-shell structure [55]. Under the efforts of researchers, the yolk-shell structure has shown promising application in nanoreactors, drug delivery and lithium ion batteries [56]. Recently, some researchers have also investigated the application of yolk-shell structures in photocatalysis [57–59].

The synthesis of yolk-shell structures usually needs a sacrificial template. In the work of Li et al., gold nanoparticles were first coated with a layer of SiO_2 by the hydrolysis of tetraethyl orthosilicate (TEOS). Next, the SiO_2 -coated gold nanoparticles were coated with a layer of TiO_2 by the hydrolysis of tetrabutyl titanate (TBOT). Then, the as-prepared gold nanoparticles were coated with a layer of SiO_2 again to protect the TiO_2 layer during the calcination process. After calcination, the two SiO_2 layers were removed by the etch of NaOH solution. Thus, the Au@TiO_2 yolk-shell nanoparticles were prepared. The SiO_2 layers served as the sacrificial template during the synthetic process [57].

3.4. Janus Structure

Janus particles, as first described by de Gennes in 1991, refer to the particles with anisotropic structure, which are composed of two distinct parts [60]. The dual nature of Janus particles endows themselves with fascinating properties, such as unique surface properties, controlled self-assembly behavior and response to multiple stimuli, etc. [61,62]. When applied in photocatalysis, Janus nanoparticles composed of metal and semiconductor can also exhibit remarkable photocatalytic properties.

Different from conventional structures, the synthesis of Janus structures needs delicate control over the combination of two distinct parts. As demonstrated by the work of Seh et al., Au/TiO_2 Janus nanoparticles were synthesized through controlled hydrolysis of titanium diisopropoxide bis(acetylacetonate) (TAA) on the surface of gold nanoparticles. The reason for choosing TAA was that

the hydrolysis rate of TAA was rather slow, which had a significant influence on the structure of the products. Thus, during the slow hydrolysis of TAA in the alkaline suspension of gold nanoparticles in isopropanol, TiO₂ combined with gold nanoparticles to form the Au/TiO₂ Janus nanoparticles [63].

3.5. Array Structure

Due to the promising application in nanodevices, the array structure has been widely researched during the past few decades [64–66]. In photocatalysis, the array structure has also been utilized to improve the photocatalytic properties of M/S nanocomposites [67].

The synthesis of array structures is mainly achieved through a template-assisted deposition process. In the work of Wang et al., an anodic aluminum oxide (AAO) template with one side deposited with a layer of gold and connected to a piece of aluminum foil was utilized as the working electrode in an electrochemical cell. For the deposition of CdS, the working electrode was biased to -2.5 V vs. standard calomel electrode (SCE) in the electrolyte of sulfur and cadmium chloride dissolved in dimethyl sulfoxide (DMSO). For the deposition of Au, the working electrode was biased to -0.95 V vs. SCE in commercial Au Orotemp 24. After alternate deposition of CdS and Au, the AAO template was removed through chemical etching. Thus, photocatalytic Au/CdS nanorod arrays were obtained [67].

3.6. Multi-Junction Structure

M/S nanocomposite photocatalysts with multi-junction structures are formed by sandwiching metal nanoparticles between two semiconductors. Thus, the electron transfer process in multi-junction M/S nanocomposite photocatalysts is very similar to that of Z-scheme photocatalytic systems in nature, which could endow them excellent photocatalytic properties [68–70].

Take the pioneer work of Tada et al. for example. The CdS/Au/TiO₂ multi-junction nanoparticles as the all-solid-state Z-scheme photocatalytic system were synthesized through a two-step deposition process. In the first step, gold was deposited on the TiO₂ nanoparticles through an impregnation process with chloroauric acid as the precursor. In the second step, cadmium sulfide was deposited on the Au/TiO₂ nanoparticles through the UV-induced reaction of sulfur and cadmium perchlorate. Thus, CdS/Au/TiO₂ multi-junction nanoparticles were prepared [71].

4. Applications and Properties of M/S Nanocomposite Photocatalysts

To date, the application areas of photocatalysis are mainly focused on environmental remediation, selective organic transformation, hydrogen evolution and disinfection.

4.1. Environmental Remediation

The photo-excited electrons and holes in semiconductor photocatalysts as well as the associated radicals possess high chemical activity, which can degrade pollutants to low- or non-hazardous substances [72–75]. As reported, most of the researches in photocatalytic environmental remediation were focused on degradation of organic pollutants such as Rhodamine B (RhB), Methylene blue (MB), methyl orange (MO) and so on. To the best of our knowledge, the only inorganic pollutant that has been involved in the research of photocatalytic environmental remediation is nitric oxide (NO). Table 1 lists some of the most representative M/S nanocomposite photocatalysts applied in environmental remediation [51,59,71,76–100].

Table 1. Metal/semiconductor (M/S) nanocomposite photocatalysts for environmental remediation.

Photocatalyst	Structure	Pollutant	Light source	Reference
Au/TiO ₂	Conventional structure	RhB	Visible light	[51]
Au/ZnO	Conventional structure	RhB, phenol red, procion red	Ultraviolet (UV) light	[76]
Au/ZnO	Conventional structure	RhB	UV light	[77]
Ag/ZnO	Conventional structure	MB	UV light	[78]
Ag/ZnO	Conventional structure	RhB	UV light	[79]
Ag/ZnO	Conventional structure	RhB	Simulated sunlight	[80]
Au/TiO ₂	Conventional structure	MB, MO, <i>p</i> -nitrophenol	Visible light	[81]
Ag/ZnO	Conventional structure	RhB	Visible light	[82]
Au/TiO ₂ , Pt/TiO ₂ , Ir/TiO ₂	Conventional structure	Azo dye	UV light	[83]
Ag/TiO ₂	Conventional structure	RhB, ciprofloxacin	Visible light	[84]
Cu/Cu ₂ O	Conventional structure	RhB, MO, MB	Visible light	[85]
Bi/amorphous bismuth oxide (A-BO)	Conventional structure	NO	Visible light	[86]
Bi/(BiO) ₂ CO ₃	Conventional structure	NO	Visible light	[87]
Bi/g-C ₃ N ₄	Conventional structure	NO	Visible light	[88]
Bi/ZnWO ₄	Conventional structure	NO	Visible light	[89]
Bi/BiOCl	Conventional structure	NO	Visible light	[90]
M@TiO ₂ (M = Au, Pd, Pt)	Core-shell structure	RhB	UV light, visible light	[91]
Au@Cu ₂ O	Core-shell structure	MO	Visible light	[92]
Au@Cu ₂ O	Core-shell structure	MO	Visible light	[93]
Au@CdS	Core-shell structure	RhB	Visible light	[94]
Au@TiO ₂	Core-shell structure	Acetaldehyde	UV light, visible light	[95]
Bi@Bi ₂ O ₃	Core-shell structure	NO	Visible light	[96]
Ag@Cu ₂ O	Core-shell structure	MO	Visible light	[97]
Au@TiO ₂	Yolk-shell structure	RhB	Visible light, simulated sunlight	[59]
Cu@CuS	Yolk-shell structure	MB	Simulated sunlight	[98]
Au/ZnO	Janus structure	RhB	UV light	[99]
Au/ZnO	Janus structure	MO	UV light	[100]
CdS/Au/TiO ₂	Multi-junction structure	Methyl viologen (MV)	UV light	[71]

Due to the facile synthesis, more than half of the M/S nanocomposite photocatalysts listed in Table 1 possess the conventional structure. In the work of Lin et al., through coupling ZnO nanofibers with Ag, the as-synthesized Ag/ZnO photocatalysts exhibited much better properties for photocatalytic degradation of RhB than pristine ZnO photocatalysts, which was revealed in Figure 5a [79]. As revealed in Figure 5b, the properties of Ag/ZnO photocatalysts did not increase linearly with the Ag loading content and reached a peak at the Ag loading content of 7.5 at%. In addition, the repeatability test results in Figure 5c manifested the attenuation of the properties of Ag/ZnO photocatalysts was negligible after three cycles. The excellent properties of Ag/ZnO photocatalysts originated from the enhanced charge separation at the Ag-ZnO interface, which was evidenced by the photoluminescence (PL) spectra in Figure 5d. Toward removal of NO, Li et al. synthesized Bi/A-BO photocatalysts which could remove NO effectively under visible light illumination [86]. The remarkable properties of Bi/A-BO photocatalysts originated from SPR of Bi which could absorb visible light effectively and enhance the charge separation in A-BO. Li et al. also utilized electron spin resonance (ESR) spectroscopy for in-situ investigation of the reactive species during the photocatalytic process. (For detailed information about utilizing ESR spectroscopy to detect radicals, these two reviews, [101,102], are recommended.) The results revealed superoxide radicals (O₂^{•-}) radicals were the major active species for photocatalytic NO oxidation.

For the M/S nanocomposite photocatalysts possessing the core-shell structure, their properties in photocatalytic environmental remediation were in strong relationship with the metal core and shell thickness. In the work of Zhang et al., the effect of Au, Pd and Pt cores on the photocatalytic activity of M@TiO₂ (M = Au, Pd and Pt) core-shell nanoparticles for degradation of RhB was investigated [91]. As revealed in Figure 6, core-shell M@TiO₂ (M = Au, Pd and Pt) exhibited different photocatalytic properties under the irradiation of UV light and visible light. Under irradiation of UV light, the photocatalytic properties of core-shell M@TiO₂ (M = Au, Pd and Pt) followed the order P25 TiO₂ > Pt@TiO₂ > Pd@TiO₂ > Au@TiO₂, while under irradiation of visible light the photocatalytic properties of core-shell M@TiO₂ (M = Au, Pd and Pt) followed the order Pd@TiO₂ > Pt@TiO₂ > Au@TiO₂ > P25 TiO₂. The results indicated the metal core had two impacts on the photocatalytic properties of core-shell M@TiO₂ (M = Au, Pd and Pt), i.e., improving charge separation at the metal-TiO₂ interface

and modulating light absorption of TiO_2 . In addition, Zhang et al. also demonstrated that the hydroxyl radicals ($\bullet\text{OH}$) generated on core-shell M@TiO_2 played a more important role than superoxide radicals and holes in degradation of RhB under irradiation of UV light, while under the irradiation of visible light holes generated on core-shell M@TiO_2 played a predominant role in degradation of RhB. The effect of shell thickness on core-shell M/S nanocomposite photocatalysts was revealed by Kong et al. [93]. In their research, the properties of core-shell $\text{Au@Cu}_2\text{O}$ photocatalysts for degradation of MO varied with the Cu_2O shell thickness in the order $127\text{ nm} > 96\text{ nm} > 197\text{ nm} > 250\text{ nm} > 158\text{ nm}$. Kong et al. thought the nonlinear relationship between the properties of core-shell $\text{Au@Cu}_2\text{O}$ photocatalysts and the shell thickness could be attributed to several factors, i.e., surface area, light absorption and scattering, charge-carrier dynamics and core-shell interactions, which competed with each other.

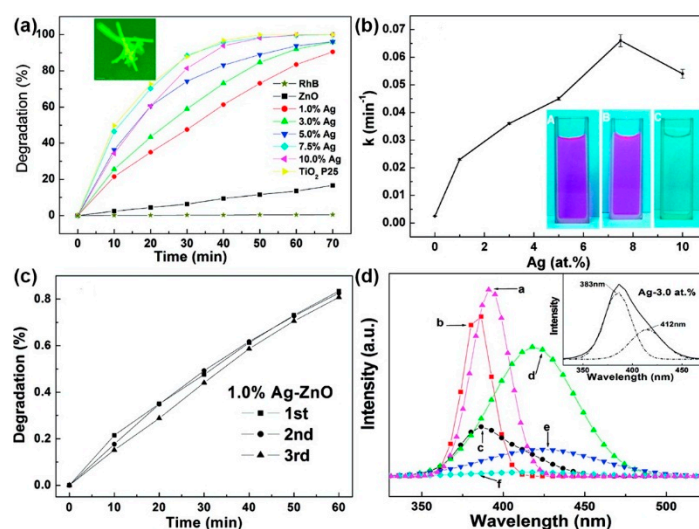


Figure 5. (a) Kinetics of the photodegradation of RhB by Ag/ZnO nanoparticles; (b) The degradation rate constant versus the Ag loading content; (c) Photodegradation of RhB by Ag/ZnO nanoparticles for three cycles; (d) PL spectra of the Ag/ZnO nanofibers with various Ag loading contents ((a) pure ZnO, (b) 1 atom% Ag, (c) 3 atom% Ag, (d) 5 atom% Ag, (e) 7.5 atom% Ag, (f) 10 atom% Ag). Reproduced from [79], with copyright permission from American Chemical Society, 2009.

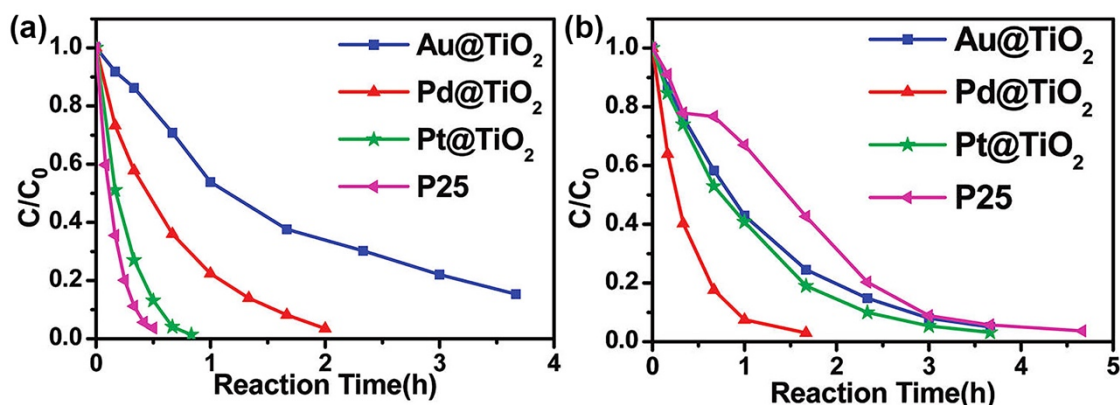


Figure 6. (a) Degradation of RhB by P25 and M@TiO_2 ($\text{M} = \text{Au}, \text{Pd}$ and Pt) under UV irradiation; (b) Degradation of RhB by P25 and M@TiO_2 ($\text{M} = \text{Au}, \text{Pd}$ and Pt) under visible light irradiation. Reproduced from [90], with copyright permission from American Chemical Society, 2011.

Compared with M/S nanocomposite photocatalysts possessing the conventional and core-shell structures, there is less research on M/S nanocomposite photocatalysts with the yolk-shell, Janus and multi-junction structures for environmental remediation. Wang et al. investigated the properties of yolk-shell Au@TiO_2 photocatalysts for degradation of RhB [59]. In their research, they also introduced

reduced graphene oxide (r-GO) into the TiO₂ shell. The results demonstrated the properties of yolk-shell Au@r-GO/TiO₂ photocatalysts were better than yolk-shell Au@TiO₂ photocatalysts, which indicated the charge separation in the TiO₂ shell increased with the electron conductivity of the TiO₂ shell. In the work of Yao et al., the properties of Janus Au/ZnO photocatalysts were investigated for degradation of MO [100]. The results demonstrated the properties of Janus Au/ZnO photocatalysts for degradation of MO were higher than that of pristine ZnO photocatalysts and increased with the size of Au nanoparticles under UV light illumination. In the pioneer work of Tada et al., multi-junction CdS/Au/TiO₂ photocatalysts were synthesized as the all-solid-state Z-scheme photocatalysts for the degradation of MV [71]. As revealed in Figure 7a, multi-junction CdS/Au/TiO₂ photocatalysts exhibited much higher properties than CdS/TiO₂, Au/TiO₂ and TiO₂ photocatalysts, which revealed the charge separation caused by TiO₂ → Au → CdS Z-scheme electron transfer was more efficient than that of the single- or double-component systems. The Z-scheme electron transfer was illustrated in Figure 7b. Besides, Tada et al. pointed out that the properties of all-solid-state Z-scheme photocatalysts could be further improved by modifying the energy band structures of the semiconductor components.

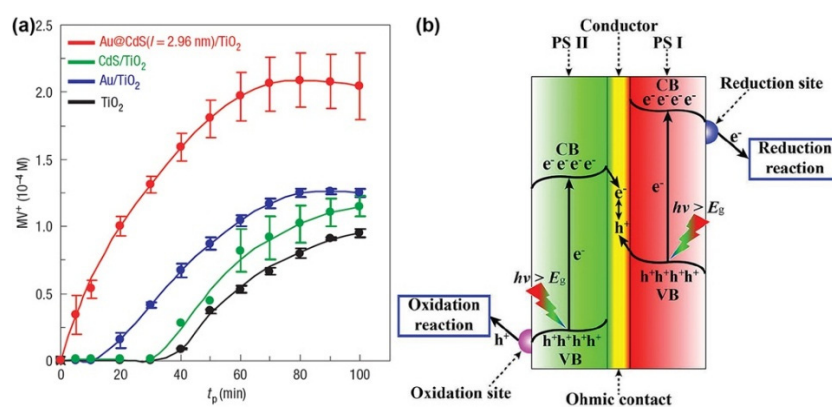


Figure 7. (a) Photocatalytic reduction of MV by TiO₂, Au/TiO₂, CdS/TiO₂ and Au@CdS/TiO₂ (CdS/Au/TiO₂). Reproduced from [71], with copyright permission from Springer Nature, 2006; (b) Schematic diagram of Z-scheme electron transfer. Reproduced from [68], with copyright permission from John Wiley & Sons, 2014.

4.2. Selective Organic Transformation

Unlike the non-selective mineralization process in environmental remediation, photocatalysis can also drive organic transformation processes to selectively synthesize valuable chemicals [103–105]. Compared with thermochemical synthetic process, the photocatalytic selective organic transformation process often requires milder conditions and shorter reaction sequences and can exclude some undesirable side reactions. Based on the reported research, the photocatalytic selective organic transformation reactions can be divided into three categories, i.e., the oxidation reaction, reduction reaction and coupling reaction [103]. In Table 2, some of the most representative M/S nanocomposite photocatalysts applied in selective organic transformation are listed [106–120].

Table 2. M/S nanocomposite photocatalysts for selective organic transformation.

Photocatalyst	Structure	Reaction Type	Reactant	Light Source	Reference
Pt/TiO ₂ , Pd/TiO ₂	Conventional structure	Oxidation reaction	Benzene	UV light	[106]
Au/TiO ₂	Conventional structure	Oxidation reaction	Benzene	Simulated sunlight	[107]
Pt/TiO ₂	Conventional structure	Oxidation reaction	Benzene	UV light	[108]
Pt/TiO ₂	Conventional structure	Oxidation reaction	(substituted) Benzene	UV light	[109]
Au/CeO ₂	Conventional structure	Oxidation reaction	Aromatic alcohols	Visible light	[110]
Pt@CeO ₂	Core-shell, yolk-shell structure	Oxidation reaction	Benzyl alcohol	Visible light	[111]
Au/TiO ₂	Janus structure	Oxidation reaction	Methanol	UV light	[112]
Ag/TiO ₂	Conventional structure	Reduction reaction	Nitrobenzene	UV light	[113]
M/TiO ₂ (M = Pt, Pd, Rh, Ag and Au)	Conventional structure	Reduction reaction	Carbon dioxide (CO ₂)	UV light	[114]
Pt-Cu/TiO ₂	Conventional structure	Reduction reaction	CO ₂	Visible light	[115]
Ag/TiO ₂	Conventional structure	Reduction reaction	CO ₂	Simulated sunlight	[116]
Ag/La ₂ Ti ₂ O ₇	Conventional structure	Reduction reaction	CO ₂	UV light	[117]
Pt/TiO ₂	Conventional structure	Reduction reaction	CO ₂	Simulated sunlight	[118]
Au-Pd/ZrO ₂	Conventional structure	Oxidation, coupling reaction	Benzylamine, benzyl alcohol etc.	Visible light	[119]
Pd/SiC	Conventional structure	Coupling reaction	Iodobenzene, phenylboronic acid	Visible light	[120]

Towards the photocatalytic selective oxidation reactions, Yuzawa et al. investigated the effect of Pt loading on the properties of Pt/TiO₂ photocatalysts for amination of benzene to aniline and unfolded the reaction mechanism governing the photocatalytic amination process [108]. As revealed in Figure 8, the conversion yield of Pt/TiO₂ did not increase linearly with the Pt loading content and reached a peak at about 0.1 wt% Pt loading content, while the aniline selectivity of Pt/TiO₂ photocatalysts was hardly influenced by the Pt loading content and remained about 97%. The mechanism governing the photocatalytic amination process was clarified through ESR spectroscopy. First, the holes on the TiO₂ surface oxidized an ammonia molecule to form a neutral amide radical, which then reacted with the aromatic ring to form an intermediate, and afterwards the hydrogen of the intermediate was abstracted by the active sites on the Pt surface, leading to the formation of aniline. Thus, it could be deduced that the charge separation at the Pt-TiO₂ interface could significantly enhance the properties of Pt/TiO₂ photocatalysts for the amination of benzene. Zhang et al. investigated the properties of core-shell and yolk-shell Pt@CeO₂ photocatalysts for oxidation of benzyl alcohol to benzaldehyde [111]. As revealed in Figure 9, core-shell Pt@CeO₂ photocatalysts exhibited much higher benzaldehyde yield and selectivity than yolk-shell Pt@CeO₂ photocatalysts. Zhang et al. attributed the unsatisfactory properties of yolk-shell Pt@CeO₂ photocatalysts to the loose contact between the Pt core and CeO₂ shell, which deteriorated the charge separation at the Pt-CeO₂ interface.

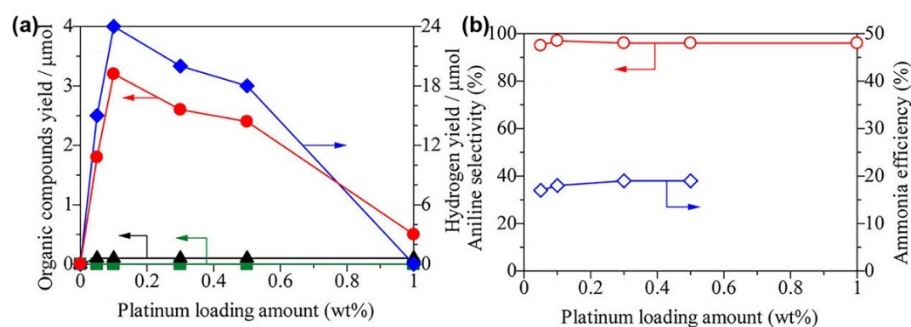


Figure 8. (a) Conversion yield of Pt/TiO₂ versus the Pt loading amount; (b) Aniline selectivity of Pt/TiO₂ versus the Pt loading amount. Reproduced from [107], with copyright permission from American Chemical Society, 2013.

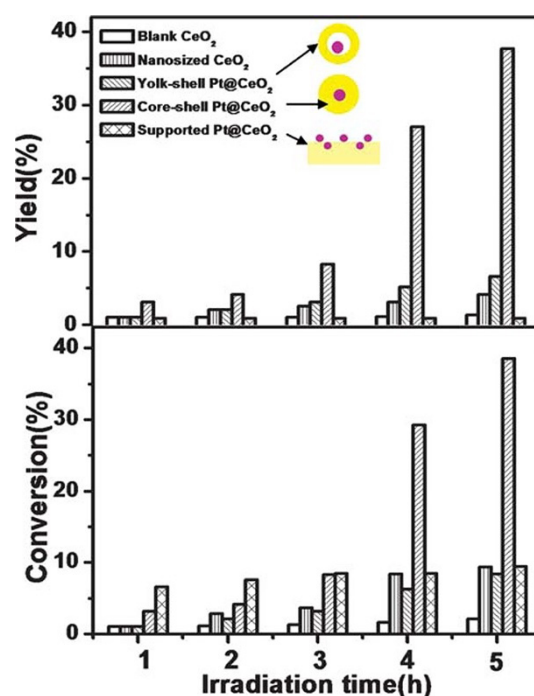


Figure 9. Results of photocatalytic selective oxidation of benzyl alcohol to benzyl aldehyde over the core-shell Pt@CeO₂, yolk-shell Pt@CeO₂, supported Pt/CeO₂, CeO₂ nanoparticles and blank CeO₂. Reproduced from [110], with copyright permission from The Royal Society of Chemistry, 2011.

As listed in Table 2, the photocatalytic selective reduction reactions mainly involve hydrogenation of nitroaromatics and reduction of CO₂. The investigation of Tada et al. on hydrogenation of nitroaromatics demonstrated that the life time of electrons could also be prolonged by the charge separation at the Ag-TiO₂ interface, leading to the enhanced properties of Ag/TiO₂ photocatalysts for hydrogenation of nitrobenzene to aniline [113]. For better properties of photocatalytic reduction of CO₂ to CH₄, Xie et al. combined P25 TiO₂ with five noble metals, i.e., Pt, Pd, Rh, Ag and Au [114]. During the photocatalytic test, the properties of M/TiO₂ photocatalysts increased in the sequence of Ag/TiO₂ < Rh/TiO₂ < Au/TiO₂ < Pd/TiO₂ < Pt/TiO₂, which indicated the charge separation at the metal-TiO₂ interface improved with the Schottky barrier height.

Towards the photocatalytic coupling reactions, Jiao et al. investigated the properties of Pd/SiC photocatalysts for Suzuki coupling of iodobenzene and phenylboronic acid [120]. Under visible light illumination, the conversion of iodobenzene and selectivity for the main product of Pd/SiC both reached nearly 100%. Jiao et al. also evaluated the effect of photogenerated electrons and holes in Pd/SiC on the Suzuki coupling process. After adding the electron-capturing agent (or hole-capturing

agent) into the reaction system, the photocatalytic properties of Pd/SiC decreased dramatically, which indicated both the photogenerated electrons and holes contributed to the Suzuki coupling process.

4.3. Hydrogen Evolution

As a significant process to convert solar energy into chemical energy, photocatalytic hydrogen evolution has always been the hot spot in the research field of photocatalysis [47,121–123]. Table 3 lists some of the most representative M/S photocatalysts for hydrogen evolution [48,63,67,124–144].

Table 3. M/S nanocomposite photocatalysts for hydrogen evolution.

Photocatalyst	Structure	Light Source	Reference
Pt/TiO ₂	Conventional structure	UV light	[27]
PtNi _x /g-C ₃ N ₄	Conventional structure	UV light	[124]
Au/TiO ₂ , Ag/TiO ₂	Conventional structure	Visible light	[125]
Cu/TiO ₂ , Ni/TiO ₂ , CuNi/TiO ₂	Conventional structure	UV light	[126]
Pt ₃ Co/CdS, Pt ₃ Co/TiO ₂	Conventional structure	UV light	[127]
Au/ZnO	Conventional structure	Simulated sunlight	[128]
Au/MoS ₂	Conventional structure	Visible light	[129]
Au/ZnO	Conventional structure	Visible light	[130]
Au/CdS	Conventional structure	Simulated sunlight	[131]
Ni/CdS	Conventional structure	UV light	[132]
Pt/TiO ₂ , Au/TiO ₂	Conventional structure	Simulated sunlight	[133]
SnRu _x /TiO ₂	Conventional structure	UV light	[134]
Au/Cu ₂ O	Conventional, core-shell structure	Visible light	[135]
Au@CdS	Core-shell structure	Visible light	[136]
Au@TiO ₂	Yolk-shell structure	UV light	[137]
Au@TiO ₂	Yolk-shell structure	UV light	[138]
Au/TiO ₂	Janus structure	Visible light	[63]
Au/CdS	Array structure	Visible light	[67]
CdS/Au/ZnO	Multi-junction structure	UV light	[139]
CdS/Au/MoS ₂	Multi-junction structure	Visible light	[140]
CdS/Pt/ZnO	Multi-junction structure	Simulated sunlight	[141]
CdS/M/TiO ₂ (M = Au, Ag, Pt, Pd)	Multi-junction structure	Simulated sunlight	[142]
CoO _x /Ir/Ta ₃ N ₅	Multi-junction structure	Simulated sunlight	[143]
Cr ₂ O ₃ /Rh/ (Ga _{1-x} Zn _x)(N _{1-x} O _x)	Multi-junction structure	Visible light	[144]

For the M/S nanocomposite photocatalysts listed in Table 3, their properties for photocatalytic hydrogen evolution achieved remarkable enhancement from the charge separation at the metal-semiconductor interface and the SPR of the metal component. In the work of Bi et al., they utilized Pt-Ni alloy nanoparticles to decorate g-C₃N₄ for saving the usage of Pt [124]. The results revealed the PtNi_x/g-C₃N₄ photocatalysts could exhibit comparable properties to that of Pt/g-C₃N₄ photocatalysts, which provided a possible approach for developing M/S nanocomposite photocatalysts with excellent properties as well as low cost. In the work of Ingram et al., the difference in the properties of Ag/TiO₂ and Au/TiO₂ (TiO₂ was doped by nitrogen atoms, i.e., N-TiO₂) photocatalysts for visible light-driven hydrogen evolution was investigated, which shed light on more effective utilization of SPR [125]. As revealed in Figure 10a, the SPR of Ag and Au was excited at the wavelengths of about 400 and 500 nm, respectively, while the absorption edge of N-TiO₂ was around 400 nm. Therefore, the SPR of Ag was more efficient for exciting electron-hole pairs in N-TiO₂ than Au, which was supported by the photocatalytic hydrogen evolution test results in Figure 10b.

Towards the core-shell and yolk-shell structure, Ma et al. investigated the effect of Au cores on the properties of core-shell Au@CdS photocatalysts for hydrogen evolution [136]. As revealed in Figure 11, under irradiation of visible light with wavelength ≥ 420 nm, core-shell Au@CdS exhibited apparently higher photocatalytic properties than pristine CdS, while under irradiation of visible light with wavelength ≥ 500 nm, the photocatalytic properties of core-shell Au@CdS were only slightly higher than pristine CdS. Thus, Ma et al. thought the radiative energy transfer from SPR-excited Au to CdS was the main contribution to the enhanced photocatalytic properties of core-shell Au@CdS, rather than the electron transfer from SPR-excited Au to CdS. In the work of Ngaw et al., the effect of Au content on the photocatalytic properties of yolk-shell Au@TiO₂ for water splitting was investigated [137]. The

photocatalytic properties of yolk-shell Au@TiO₂ also did not improve linearly with the Au content under the irradiation of both visible light and UV light, and reached a peak at 2 wt% Au content. In addition, Ngaw et al. ascribed the enhanced photocatalytic properties of yolk-shell Au@TiO₂ to the void space and highly porous shell in yolk-shell Au@TiO₂, which provided more active sites for H⁺ ions to be reduced and more channels for reactants to diffuse into and out of the photocatalytic particles.

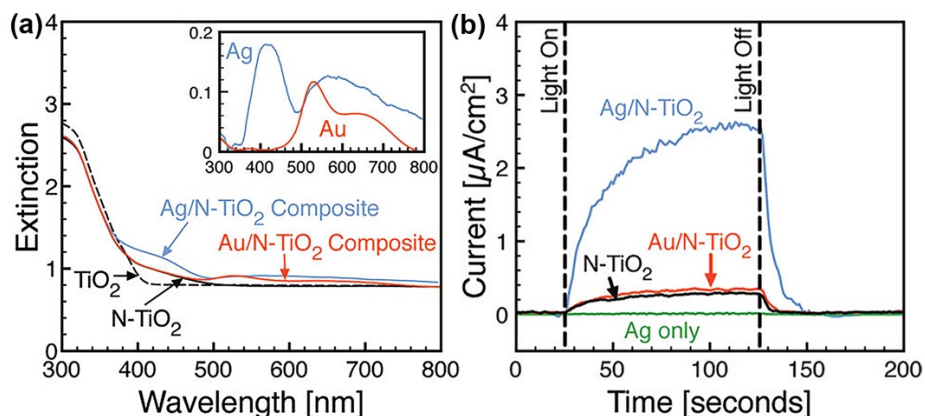


Figure 10. (a) Ultraviolet-visible extinction spectra of TiO₂, N-TiO₂, Ag/N-TiO₂ and Au/N-TiO₂ samples. The inset shows difference spectra for Ag and Au (i.e., the Ag/N-TiO₂ or Au/N-TiO₂ spectrum minus the N-TiO₂ spectrum); (b) Photocurrent responses (per macroscopic electrode area) under visible light illumination. Reproduced from [124], with copyright permission from American Chemical Society, 2011.

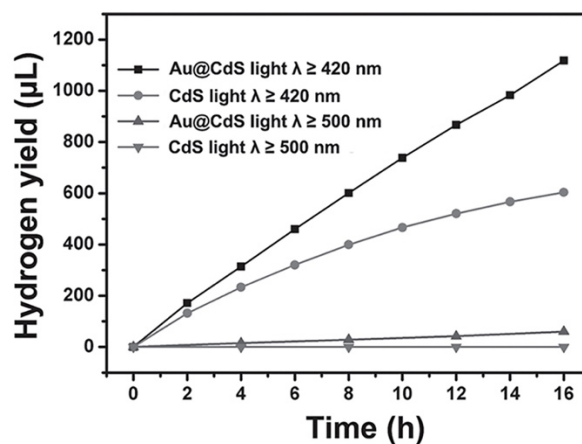


Figure 11. Photocatalytic water splitting of core-shell Au@CdS and CdS nanoparticles under irradiation of visible light with wavelength more than 420 nm and 500 nm, respectively. Reproduced from [133], with copyright permission from John Wiley & Sons, 2014.

In the work of Seh et al., the properties of Janus Au/TiO₂ and core-shell Au@TiO₂ photocatalysts for hydrogen evolution were compared and investigated [63]. As revealed in Figure 12a,b, Janus Au/TiO₂ photocatalysts exhibited higher properties than core-shell Au@TiO₂ photocatalysts and the properties of Janus Au/TiO₂ photocatalysts increased with the size of Au nanoparticles. Moreover, Seh et al. attributed the enhanced charge separation in Janus Au/TiO₂ photocatalysts to the strong plasmonic near-fields localized closely to the Au-TiO₂ interface, which was supported by the discrete-dipole approximation simulation results.

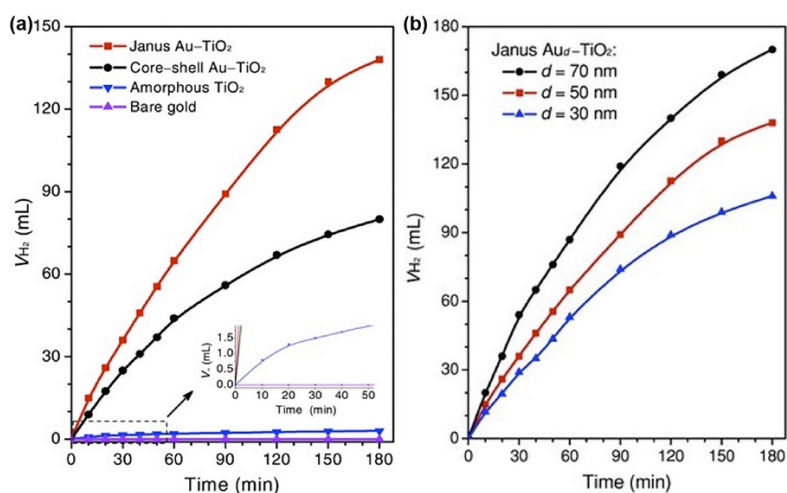


Figure 12. (a) Hydrogen evolution through photocatalytic water splitting on Janus Au/TiO₂, core-shell Au@TiO₂, amorphous TiO₂ and pristine Au nanoparticles; (b) Hydrogen evolution through photocatalytic water splitting on Janus Au/TiO₂ with different Au nanoparticle sizes. Reproduced from [63], with copyright permission from John Wiley & Sons, 2012.

As for the array structure, Wang et al. demonstrated the excellent properties of multi-segmented Au/CdS nanorod arrays (NRAs) for photocatalytic hydrogen evolution [67]. As revealed in Figure 13a, the activities of Au/CdS NRAs for hydrogen evolution increased with the number of Au-CdS segments under irradiation of simulated sunlight. In addition, compared with pristine CdS NRAs, the activities of Au/CdS NRAs for hydrogen evolution gained significant enhancement under irradiation of simulated sunlight, which was presented in Figure 13b. Wang et al. attributed the excellent properties of Au/CdS NRAs for hydrogen evolution to the charge separation at the Au-CdS interface under irradiation of simulated sunlight.

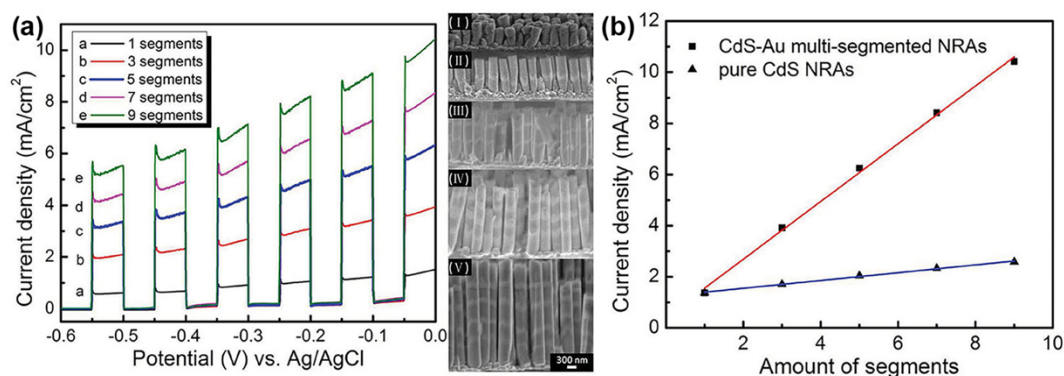


Figure 13. (a) Hydrogen evolution on the multi-segmented CdS/Au NRAs in the photoelectrochemical cell under irradiation of simulated sun light. (I-V) SEM images of the side view of the CdS-Au NRAs. (b) Comparison of the activities for hydrogen evolution on the CdS/Au NRAs and pristine CdS NRAs under irradiation of simulated sunlight. Reproduced from [67], with copyright permission from John Wiley & Sons, 2014.

Toward the multi-junction structure, Yu et al. demonstrated the excellent properties of multi-junction CdS/Au/ZnO photocatalysts for hydrogen evolution [139]. To reveal the high charge separation efficiency bought by the Z-scheme electron transfer, Yu et al. also synthesized Au/CdS/ZnO photocatalysts by depositing Au on CdS/ZnO photocatalysts. As shown in Figure 14a, the properties of multi-junction CdS/Au/ZnO photocatalysts was 4.5 times higher than that of CdS/ZnO photocatalysts, while the properties of Au/CdS/ZnO photocatalysts achieved only a small enhancement compared with CdS/ZnO photocatalysts. The PL spectra in Figure 14b further

confirmed the high charge separation efficiency due to the Z-scheme electron transfer in multi-junction CdS/Au/ZnO photocatalysts.

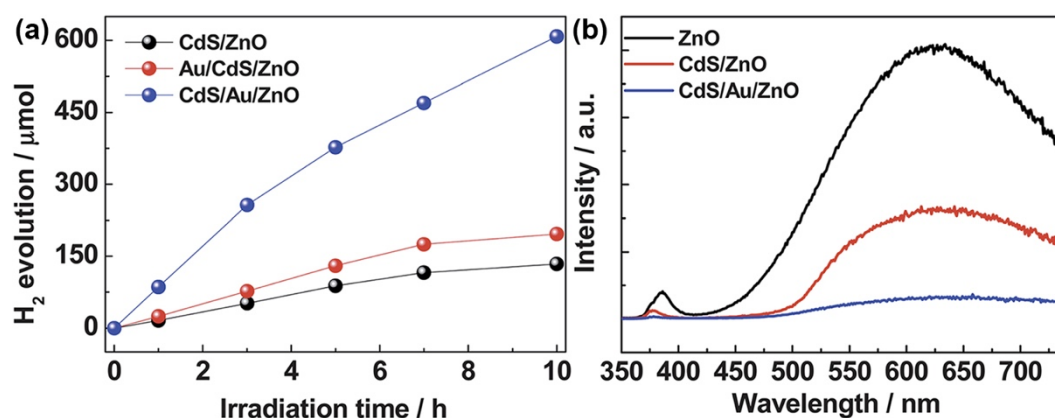


Figure 14. (a) Hydrogen evolution through photocatalytic water splitting on CdS/ZnO, Au/CdS/ZnO and CdS/Au/ZnO, respectively. (b) PL spectra of ZnO, CdS/ZnO and CdS/Au/ZnO at a 270 nm excitation wavelength. Reproduced from [136], with copyright permission from The Royal Society of Chemistry, 2013.

4.4. Disinfection

In 1985, Matsunaga et al. first reported the photocatalytic inactivation of bacteria on the surface of TiO₂ [145]. Since then, a lot of research has been devoted to the photocatalytic inactivation of microorganisms such as bacteria, viruses, protozoa and so on [18,146–150]. Furthermore, due to the nonexistence of secondary pollution, photocatalytic disinfection is a promising alternative approach for water purification. Table 4 lists some of the most representative M/S nanocomposite photocatalysts for disinfection [151–159].

Table 4. M/S nanocomposite photocatalysts for disinfection.

Photocatalyst	Structure	Bacteria	Light Source	Reference
Ag/g-C ₃ N ₄	Conventional structure	<i>Escherichia coli</i>	UV and visible light	[151]
Ag/TiO ₂	Conventional structure	<i>Escherichia coli</i>	UV light	[152]
Ag/TiO ₂	Conventional structure	<i>Escherichia coli</i>	Sunlight	[153]
Ag/TiO ₂	Conventional structure	<i>Escherichia coli</i>	Simulated sunlight	[154]
Cu/TiO ₂	Conventional structure	<i>Escherichia coli</i>	UV and visible light	[155]
Ag/BiOI	Conventional structure	<i>Escherichia coli</i>	Visible light	[156]
Ag/AgX (X = Cl, Br, I)	Conventional structure	<i>Escherichia coli</i>	Visible light	[157]
Ag/ZnO	Conventional structure	<i>Escherichia coli</i>	Visible light	[158]
Ag@ZnO	Core-shell structure	<i>Vibrio cholerae</i>	Sunlight	[159]

Taking into account the practical application of photocatalytic disinfection for water purification, most of the light sources involved in the research are visible light as revealed in Table 4. Therefore, the enhanced properties of M/S nanocomposite photocatalysts for disinfection are mainly attributed to the SPR of the metal component. In the work of Shi et al., due to the SPR of Ag, the Ag/AgX (X = Cl, Br, I) photocatalysts exhibited remarkable properties for the inactivation of *Escherichia coli* under visible light illumination [157]. Shi et al. also evaluated the contribution of different photo-generated reactive species to the disinfection process by adding scavengers into the reaction system. The results indicated holes are the dominant reactive species over other reactive species such as electrons, •OH, H₂O₂ and so on.

5. Conclusions and Perspectives

In this review, we demonstrate the properties of M/S nanocomposite photocatalysts in relation to their structures for application in environmental remediation, selective organic

transformation, hydrogen evolution and disinfection. Due to the enhanced charge separation at the metal-semiconductor interface and increased absorption of visible light induced by the SPR of metals, M/S nanocomposite photocatalysts usually exhibit much better properties than pristine semiconductor photocatalysts.

For future development of M/S nanocomposite photocatalysts, our perspectives can be summarized as the following four points:

- (1) To date, most of metals utilized to combine with semiconductor photocatalysts are noble metals, which are scarce in nature and expensive. To save the use of noble metals, coupling semiconductors with alloys composed of noble and non-noble metals is highly recommended. In addition, due to the non-linear relationship between the properties of M/S nanocomposite photocatalysts and metal loading, precise control over the metal loading in the M/S nanocomposite photocatalysts deserve further research.
- (2) For more efficient utilization of SPR to enhance the properties of M/S nanocomposite photocatalysts, the SPR excitation wavelength of the metal nanoparticles should overlap the absorption edge of the semiconductor nanoparticles, which could be achieved by changing the shape and particle size of the metal nanoparticles and modulating the band structure of the semiconductor nanoparticles.
- (3) Synergistic utilization of enhanced charge separation at the metal-semiconductor interface and SPR of metals might endow the M/S nanocomposite photocatalysts with even better properties under visible light illumination, because the SPR-induced charge separation in M/S nanocomposite photocatalysts could be further enhanced by introducing another metal co-catalyst with large work function to the M/S nanocomposite photocatalysts.
- (4) Due to their intrinsic ability to prohibit particle agglomeration, the core-shell, yolk-shell and array structures (especially the array structure) might be the ideal structures for M/S nanocomposite photocatalysts. Therefore, there exists a strong demand for more facile synthesis of these structures.

Author Contributions: Y.-s.F., J.L. and J.G.L. conceptualized this review; Y.-s.F. collected and analyzed the data; Y.-s.F. and J.L. wrote the paper.

Funding: This research was funded by National Key Research & Development Program of China through the grant number 2017YFB0305300 and Joint Funds of the National Natural Science Foundation of China through the grant number U1660203.

Acknowledgments: The authors would like to thank Tao Deng and Jianbo Wu for their valuable suggestions to this review.

Conflicts of Interest: The authors declare no conflict of interest.

References

1. Fujishima, A.; Honda, K. Electrochemical Photolysis of Water at a Semiconductor Electrode. *Nature* **1972**, *238*, 37. [[CrossRef](#)] [[PubMed](#)]
2. Huang, Y.; Sun, F.; Wang, H.; He, Y.; Li, L.; Huang, Z.; Wu, Q.; Yu, J.C. Photochemical growth of cadmium-rich CdS nanotubes at the air–water interface and their use in photocatalysis. *J. Mater. Chem.* **2009**, *19*, 6901–6906. [[CrossRef](#)]
3. Wang, S.; Wang, X. Photocatalytic CO₂ reduction by CdS promoted with a zeolitic imidazolate framework. *Appl. Catal. B Environ.* **2015**, *162*, 494–500. [[CrossRef](#)]
4. An, X.; Yu, X.; Yu, J.C.; Zhang, G. CdS nanorods/reduced graphene oxide nanocomposites for photocatalysis and electrochemical sensing. *J. Mater. Chem. A* **2013**, *1*, 5158–5164. [[CrossRef](#)]
5. Wang, Y.; Shi, R.; Lin, J.; Zhu, Y. Enhancement of photocurrent and photocatalytic activity of ZnO hybridized with graphite-like C₃N₄. *Energy Environ. Sci.* **2011**, *4*, 2922–2929. [[CrossRef](#)]
6. McLaren, A.; Valdes-Solis, T.; Li, G.; Tsang, S.C. Shape and Size Effects of ZnO Nanocrystals on Photocatalytic Activity. *J. Am. Chem. Soc.* **2009**, *131*, 12540–12541. [[CrossRef](#)] [[PubMed](#)]

7. Elmolla, E.S.; Chaudhuri, M. Degradation of amoxicillin, ampicillin and cloxacillin antibiotics in aqueous solution by the UV/ZnO photocatalytic process. *J. Hazard. Mater.* **2010**, *173*, 445–449. [[CrossRef](#)] [[PubMed](#)]
8. Miyauchi, M.; Takashio, M.; Tobimatsu, H. Photocatalytic Activity of SrTiO₃ Codoped with Nitrogen and Lanthanum under Visible Light Illumination. *Langmuir* **2004**, *20*, 232–236. [[CrossRef](#)] [[PubMed](#)]
9. Konta, R.; Ishii, T.; Kato, H.; Kudo, A. Photocatalytic Activities of Noble Metal Ion Doped SrTiO₃ under Visible Light Irradiation. *J. Phys. Chem. B* **2004**, *108*, 8992–8995. [[CrossRef](#)]
10. Ye, S.; Wang, R.; Wu, M.-Z.; Yuan, Y.-P. A review on g-C₃N₄ for photocatalytic water splitting and CO₂ reduction. *Appl. Surf. Sci.* **2015**, *358*, 15–27. [[CrossRef](#)]
11. Lam, S.-M.; Sin, J.-C.; Mohamed, A.R. A review on photocatalytic application of g-C₃N₄/semiconductor (CNS) nanocomposites towards the erasure of dyeing wastewater. *Mater. Sci. Semicond. Process.* **2016**, *47*, 62–84. [[CrossRef](#)]
12. Li, J.; Wu, N. Semiconductor-based photocatalysts and photoelectrochemical cells for solar fuel generation: A review. *Catal. Sci. Technol.* **2015**, *5*, 1360–1384. [[CrossRef](#)]
13. Wang, Y.; Wang, Q.; Zhan, X.; Wang, F.; Safdar, M.; He, J. Visible light driven type II heterostructures and their enhanced photocatalysis properties: A review. *Nanoscale* **2013**, *5*, 8326–8339. [[CrossRef](#)] [[PubMed](#)]
14. Montini, T.; Melchionna, M.; Monai, M.; Fornasiero, P. Fundamentals and Catalytic Applications of CeO₂-Based Materials. *Chem. Rev.* **2016**, *116*, 5987–6041. [[CrossRef](#)] [[PubMed](#)]
15. Rao, P.M.; Cai, L.; Liu, C.; Cho, I.S.; Lee, C.H.; Weisse, J.M.; Yang, P.; Zheng, X. Simultaneously Efficient Light Absorption and Charge Separation in WO₃/BiVO₄ Core/Shell Nanowire Photoanode for Photoelectrochemical Water Oxidation. *Nano Lett.* **2014**, *14*, 1099–1105. [[CrossRef](#)] [[PubMed](#)]
16. Wang, H.; Zhang, L.; Chen, Z.; Hu, J.; Li, S.; Wang, Z.; Liu, J.; Wang, X. Semiconductor heterojunction photocatalysts: Design, construction, and photocatalytic performances. *Chem. Soc. Rev.* **2014**, *43*, 5234–5244. [[CrossRef](#)] [[PubMed](#)]
17. Daghrir, R.; Drogui, P.; Robert, D. Modified TiO₂ For Environmental Photocatalytic Applications: A Review. *Ind. Eng. Chem. Res.* **2013**, *52*, 3581–3599. [[CrossRef](#)]
18. Dong, S.; Feng, J.; Fan, M.; Pi, Y.; Hu, L.; Han, X.; Liu, M.; Sun, J.; Sun, J. Recent developments in heterogeneous photocatalytic water treatment using visible light-responsive photocatalysts: A review. *RSC Adv.* **2015**, *5*, 14610–14630. [[CrossRef](#)]
19. Burda, C.; Lou, Y.; Chen, X.; Samia, A.C.S.; Stout, J.; Gole, J.L. Enhanced Nitrogen Doping in TiO₂ Nanoparticles. *Nano Lett.* **2003**, *3*, 1049–1051. [[CrossRef](#)]
20. Yu, J.C.; Yu, J.; Ho, W.; Zhang, J. Effects of F- Doping on the Photocatalytic Activity and Microstructures of Nanocrystalline TiO₂ Powders. *Chem. Mater.* **2002**, *14*, 3808–3816. [[CrossRef](#)]
21. Liu, L.; Ouyang, S.; Ye, J. Gold-Nanorod-Photosensitized Titanium Dioxide with Wide-Range Visible-Light Harvesting Based on Localized Surface Plasmon Resonance. *Angew. Chem.* **2013**, *125*, 6821–6825. [[CrossRef](#)]
22. Zhang, M.; Chen, C.; Ma, W.; Zhao, J. Visible-Light-Induced Aerobic Oxidation of Alcohols in a Coupled Photocatalytic System of Dye-Sensitized TiO₂ and TEMPO. *Angew. Chem. Int. Ed.* **2008**, *47*, 9730–9733. [[CrossRef](#)] [[PubMed](#)]
23. Asahi, R.; Morikawa, T.; Ohwaki, T.; Aoki, K.; Taga, Y. Visible-Light Photocatalysis in Nitrogen-Doped Titanium Oxides. *Science* **2001**, *293*, 269. [[CrossRef](#)] [[PubMed](#)]
24. Dhanalakshmi, K.B.; Latha, S.; Anandan, S.; Maruthamuthu, P. Dye sensitized hydrogen evolution from water. *Int. J. Hydrogen Energy* **2001**, *26*, 669–674. [[CrossRef](#)]
25. Youngblood, W.J.; Lee, S.-H.A.; Maeda, K.; Mallouk, T.E. Visible Light Water Splitting Using Dye-Sensitized Oxide Semiconductors. *Acc. Chem. Res.* **2009**, *42*, 1966–1973. [[CrossRef](#)] [[PubMed](#)]
26. Zhang, X.; Peng, T.; Song, S. Recent advances in dye-sensitized semiconductor systems for photocatalytic hydrogen production. *J. Mater. Chem. A* **2016**, *4*, 2365–2402. [[CrossRef](#)]
27. Khaki, M.R.D.; Shafeeyan, M.S.; Raman, A.A.A.; Daud, W.M.A.W. Application of doped photocatalysts for organic pollutant degradation—A review. *J. Environ. Manag.* **2017**, *198*, 78–94. [[CrossRef](#)] [[PubMed](#)]
28. Wu, N. Plasmonic metal–semiconductor photocatalysts and photoelectrochemical cells: A review. *Nanoscale* **2018**, *10*, 2679–2696. [[CrossRef](#)] [[PubMed](#)]
29. Linic, S.; Christopher, P.; Ingram, D.B. Plasmonic-metal nanostructures for efficient conversion of solar to chemical energy. *Nat. Mater.* **2011**, *10*, 911. [[CrossRef](#)] [[PubMed](#)]

30. Marschall, R. Semiconductor Composites: Strategies for Enhancing Charge Carrier Separation to Improve Photocatalytic Activity. *Adv. Funct. Mater.* **2014**, *24*, 2421–2440. [[CrossRef](#)]
31. Qu, Y.; Duan, X. Progress, challenge and perspective of heterogeneous photocatalysts. *Chem. Soc. Rev.* **2013**, *42*, 2568–2580. [[CrossRef](#)] [[PubMed](#)]
32. Schneider, J.; Bahnemann, D.; Ye, J.; Li, G. *Photocatalysis: Fundamentals and Perspectives*; Royal Society of Chemistry: London, UK, 2016. [[CrossRef](#)]
33. Castellote, M.; Bengtsson, N. Principles of TiO₂ Photocatalysis. In *Applications of Titanium Dioxide Photocatalysis to Construction Materials: State-of-the-Art Report of the RILEM Technical Committee 194-TDP*; Ohama, Y., Van Gemert, D., Eds.; Springer: Dordrecht, The Netherlands, 2011; pp. 5–10. [[CrossRef](#)]
34. Peter, L.M. CHAPTER 1 Photoelectrochemistry: From Basic Principles to Photocatalysis. In *Photocatalysis: Fundamentals and Perspectives*; The Royal Society of Chemistry: London, UK, 2016; pp. 1–28. [[CrossRef](#)]
35. Mills, A.; Le Hunte, S. An overview of semiconductor photocatalysis. *J. Photochem. Photobiol. A Chem.* **1997**, *108*, 1–35. [[CrossRef](#)]
36. Chen, S.; Wang, L.-W. Thermodynamic Oxidation and Reduction Potentials of Photocatalytic Semiconductors in Aqueous Solution. *Chem. Mater.* **2012**, *24*, 3659–3666. [[CrossRef](#)]
37. Ohtani, B. Revisiting the fundamental physical chemistry in heterogeneous photocatalysis: Its thermodynamics and kinetics. *Phys. Chem. Chem. Phys.* **2014**, *16*, 1788–1797. [[CrossRef](#)] [[PubMed](#)]
38. Liu, B.; Zhao, X.; Terashima, C.; Fujishima, A.; Nakata, K. Thermodynamic and kinetic analysis of heterogeneous photocatalysis for semiconductor systems. *Phys. Chem. Chem. Phys.* **2014**, *16*, 8751–8760. [[CrossRef](#)] [[PubMed](#)]
39. Zhang, Z.; Yates, J.T. Band Bending in Semiconductors: Chemical and Physical Consequences at Surfaces and Interfaces. *Chem. Rev.* **2012**, *112*, 5520–5551. [[CrossRef](#)] [[PubMed](#)]
40. Kamat, P.V. Manipulation of Charge Transfer Across Semiconductor Interface. A Criterion That Cannot Be Ignored in Photocatalyst Design. *J. Phys. Chem. Lett.* **2012**, *3*, 663–672. [[CrossRef](#)] [[PubMed](#)]
41. Cai, Y.-Y.; Li, X.-H.; Zhang, Y.-N.; Wei, X.; Wang, K.-X.; Chen, J.-S. Highly Efficient Dehydrogenation of Formic Acid over a Palladium-Nanoparticle-Based Mott–Schottky Photocatalyst. *Angew. Chem.* **2013**, *125*, 12038–12041. [[CrossRef](#)]
42. Liu, Y.; Gu, X.; Qi, W.; Zhu, H.; Shan, H.; Chen, W.L.; Tao, P.; Song, C.Y.; Shang, W.; Deng, T.; et al. Enhancing the Photocatalytic Hydrogen Evolution Performance of a Metal/Semiconductor Catalyst through Modulation of the Schottky Barrier Height by Controlling the Orientation of the Interface. *ACS Appl. Mater. Interfaces* **2017**, *9*, 12494–12500. [[CrossRef](#)] [[PubMed](#)]
43. Yang, J.H.; Wang, D.G.; Han, H.X.; Li, C. Roles of Cocatalysts in Photocatalysis and Photoelectrocatalysis. *Accounts Chem. Res.* **2013**, *46*, 1900–1909. [[CrossRef](#)] [[PubMed](#)]
44. Kubacka, A.; Fernández-García, M.; Colón, G. Advanced Nanoarchitectures for Solar Photocatalytic Applications. *Chem. Rev.* **2012**, *112*, 1555–1614. [[CrossRef](#)] [[PubMed](#)]
45. Teoh, W.Y.; Scott, J.A.; Amal, R. Progress in Heterogeneous Photocatalysis: From Classical Radical Chemistry to Engineering Nanomaterials and Solar Reactors. *J. Phys. Chem. Lett.* **2012**, *3*, 629–639. [[CrossRef](#)] [[PubMed](#)]
46. Hou, W.; Cronin, S.B. A Review of Surface Plasmon Resonance-Enhanced Photocatalysis. *Adv. Funct. Mater.* **2013**, *23*, 1612–1619. [[CrossRef](#)]
47. Warren, S.C.; Thimsen, E. Plasmonic solar water splitting. *Energy Environ. Sci.* **2012**, *5*, 5133–5146. [[CrossRef](#)]
48. Yu, J.; Qi, L.; Jaroniec, M. Hydrogen Production by Photocatalytic Water Splitting over Pt/TiO₂ Nanosheets with Exposed (001) Facets. *J. Phys. Chem. C* **2010**, *114*, 13118–13125. [[CrossRef](#)]
49. Lin, C.-H.; Chao, J.-H.; Liu, C.-H.; Chang, J.-C.; Wang, F.-C. Effect of Calcination Temperature on the Structure of a Pt/TiO₂ (B) Nanofiber and Its Photocatalytic Activity in Generating H₂. *Langmuir* **2008**, *24*, 9907–9915. [[CrossRef](#)] [[PubMed](#)]
50. Wu, G.; Chen, T.; Su, W.; Zhou, G.; Zong, X.; Lei, Z.; Li, C. H₂ production with ultra-low CO selectivity via photocatalytic reforming of methanol on Au/TiO₂ catalyst. *Int. J. Hydrogen Energy* **2008**, *33*, 1243–1251. [[CrossRef](#)]
51. Shi, H.; Wang, X.; Zheng, M.; Wu, X.; Chen, Y.; Yang, Z.; Zhang, G.; Duan, H. Hot-Electrons Mediated Efficient Visible-Light Photocatalysis of Hierarchical Black Au-TiO₂ Nanorod Arrays on Flexible Substrate. *Adv. Mater. Interfaces* **2016**, *3*, 1600588. [[CrossRef](#)]
52. Ghosh Chaudhuri, R.; Paria, S. Core/Shell Nanoparticles: Classes, Properties, Synthesis Mechanisms, Characterization, and Applications. *Chem. Rev.* **2012**, *112*, 2373–2433. [[CrossRef](#)] [[PubMed](#)]

53. Zhang, N.; Liu, S.Q.; Xu, Y.J. Recent progress on metal core@semiconductor shell nanocomposites as a promising type of photocatalyst. *Nanoscale* **2012**, *4*, 2227–2238. [[CrossRef](#)] [[PubMed](#)]
54. Sudeep, P.K.; Takechi, K.; Kamat, P.V. Harvesting photons in the infrared. Electron injection from excited tricarbocyanine dye (IR-125) into TiO₂ and Ag@TiO₂ core-shell nanoparticles. *J. Phys. Chem. C* **2007**, *111*, 488–494. [[CrossRef](#)]
55. Kamata, K.; Lu, Y.; Xia, Y.N. Synthesis and characterization of monodispersed core-shell spherical colloids with movable cores. *J. Am. Chem. Soc.* **2003**, *125*, 2384–2385. [[CrossRef](#)] [[PubMed](#)]
56. Liu, J.; Qiao, S.Z.; Chen, J.S.; Lou, X.W.; Xing, X.R.; Lu, G.Q. Yolk/shell nanoparticles: New platforms for nanoreactors, drug delivery and lithium-ion batteries. *Chem. Commun.* **2011**, *47*, 12578–12591. [[CrossRef](#)] [[PubMed](#)]
57. Li, A.; Zhang, P.; Chang, X.; Cai, W.; Wang, T.; Gong, J. Gold Nanorod@TiO₂ Yolk-Shell Nanostructures for Visible-Light-Driven Photocatalytic Oxidation of Benzyl Alcohol. *Small* **2015**, *11*, 1892–1899. [[CrossRef](#)] [[PubMed](#)]
58. Tu, W.; Zhou, Y.; Li, H.; Li, P.; Zou, Z. Au@TiO₂ yolk-shell hollow spheres for plasmon-induced photocatalytic reduction of CO₂ to solar fuel via a local electromagnetic field. *Nanoscale* **2015**, *7*, 14232–14236. [[CrossRef](#)] [[PubMed](#)]
59. Wang, M.; Han, J.; Xiong, H.; Guo, R. Yolk@Shell Nanoarchitecture of Au@r-GO/TiO₂ Hybrids as Powerful Visible Light Photocatalysts. *Langmuir* **2015**, *31*, 6220–6228. [[CrossRef](#)] [[PubMed](#)]
60. de Gennes, P.-G. Soft Matter (Nobel Lecture). *Angew. Chem. Int. Ed.* **1992**, *31*, 842–845. [[CrossRef](#)]
61. Lattuada, M.; Hatton, T.A. Synthesis, properties and applications of Janus nanoparticles. *Nano Today* **2011**, *6*, 286–308. [[CrossRef](#)]
62. Walther, A.; Müller, A.H.E. Janus Particles: Synthesis, Self-Assembly, Physical Properties, and Applications. *Chem. Rev.* **2013**, *113*, 5194–5261. [[CrossRef](#)] [[PubMed](#)]
63. Seh, Z.W.; Liu, S.; Low, M.; Zhang, S.-Y.; Liu, Z.; Mlayah, A.; Han, M.-Y. Janus Au-TiO₂ Photocatalysts with Strong Localization of Plasmonic Near-Fields for Efficient Visible-Light Hydrogen Generation. *Adv. Mater.* **2012**, *24*, 2310–2314. [[CrossRef](#)] [[PubMed](#)]
64. Wang, Z.L.; Song, J. Piezoelectric Nanogenerators Based on Zinc Oxide Nanowire Arrays. *Science* **2006**, *312*, 242–246. [[CrossRef](#)] [[PubMed](#)]
65. Zhu, K.; Neale, N.R.; Miedaner, A.; Frank, A.J. Enhanced Charge-Collection Efficiencies and Light Scattering in Dye-Sensitized Solar Cells Using Oriented TiO₂ Nanotubes Arrays. *Nano Lett.* **2007**, *7*, 69–74. [[CrossRef](#)] [[PubMed](#)]
66. Lin, H.-W.; Lu, Y.-J.; Chen, H.-Y.; Lee, H.-M.; Gwo, S. InGaN/GaN nanorod array white light-emitting diode. *Appl. Phys. Lett.* **2010**, *97*, 073101.
67. Wang, X.; Liow, C.; Qi, D.; Zhu, B.; Leow, W.R.; Wang, H.; Xue, C.; Chen, X.; Li, S. Programmable Photo-Electrochemical Hydrogen Evolution Based on Multi-Segmented CdS-Au Nanorod Arrays. *Adv. Mater.* **2014**, *26*, 3506–3512. [[CrossRef](#)] [[PubMed](#)]
68. Zhou, P.; Yu, J.G.; Jaroniec, M. All-Solid-State Z-Scheme Photocatalytic Systems. *Adv. Mater.* **2014**, *26*, 4920–4935. [[CrossRef](#)] [[PubMed](#)]
69. Low, J.; Jiang, C.; Cheng, B.; Wageh, S.; Al-Ghamdi, A.A.; Yu, J. A Review of Direct Z-Scheme Photocatalysts. *Small Methods* **2017**, *1*, 1700080. [[CrossRef](#)]
70. Qi, K.; Cheng, B.; Yu, J.; Ho, W. A review on TiO₂-based Z-scheme photocatalysts. *Chin. J. Catal.* **2017**, *38*, 1936–1955. [[CrossRef](#)]
71. Tada, H.; Mitsui, T.; Kiyonaga, T.; Akita, T.; Tanaka, K. All-solid-state Z-scheme in CdS–Au–TiO₂ three-component nanojunction system. *Nat. Mater.* **2006**, *5*, 782. [[CrossRef](#)] [[PubMed](#)]
72. McCullagh, C.; Skillen, N.; Adams, M.; Robertson, P.K.J. Photocatalytic reactors for environmental remediation: A review. *J. Chem. Technol. Biotechnol.* **2011**, *86*, 1002–1017. [[CrossRef](#)]
73. Khin, M.M.; Nair, A.S.; Babu, V.J.; Murugan, R.; Ramakrishna, S. A review on nanomaterials for environmental remediation. *Energy Environ. Sci.* **2012**, *5*, 8075–8109. [[CrossRef](#)]
74. Singh, S.; Mahalingam, H.; Singh, P.K. Polymer-supported titanium dioxide photocatalysts for environmental remediation: A review. *Appl. Catal. A Gen.* **2013**, *462–463*, 178–195. [[CrossRef](#)]
75. Hoffmann, M.R.; Martin, S.T.; Choi, W.; Bahnemann, D.W. Environmental applications of semiconductor photocatalysis. *Chem. Rev.* **1995**, *95*, 69–96. [[CrossRef](#)]

76. Tahir, M.N.; Natalio, F.; Cambaz, M.A.; Panthöfer, M.; Branscheid, R.; Kolb, U.; Tremel, W. Controlled synthesis of linear and branched Au@ZnO hybrid nanocrystals and their photocatalytic properties. *Nanoscale* **2013**, *5*, 9944–9949. [[CrossRef](#)] [[PubMed](#)]
77. Chen, Y.; Zeng, D.; Zhang, K.; Lu, A.; Wang, L.; Peng, D.-L. Au–ZnO hybrid nanoflowers, nanomultipods and nanopyramids: One-pot reaction synthesis and photocatalytic properties. *Nanoscale* **2014**, *6*, 874–881. [[CrossRef](#)] [[PubMed](#)]
78. Ren, C.; Yang, B.; Wu, M.; Xu, J.; Fu, Z.; Lv, Y.; Guo, T.; Zhao, Y.; Zhu, C. Synthesis of Ag/ZnO nanorods array with enhanced photocatalytic performance. *J. Hazard. Mater.* **2010**, *182*, 123–129. [[CrossRef](#)] [[PubMed](#)]
79. Lin, D.; Wu, H.; Zhang, R.; Pan, W. Enhanced Photocatalysis of Electrospun Ag–ZnO Heterostructured Nanofibers. *Chem. Mater.* **2009**, *21*, 3479–3484. [[CrossRef](#)]
80. Georgekutty, R.; Seery, M.K.; Pillai, S.C. A highly efficient Ag-ZnO photocatalyst: Synthesis, properties, and mechanism. *J. Phys. Chem. C* **2008**, *112*, 13563–13570. [[CrossRef](#)]
81. Kochuveedu, S.T.; Kim, D.-P.; Kim, D.H. Surface-Plasmon-Induced Visible Light Photocatalytic Activity of TiO₂ Nanospheres Decorated by Au Nanoparticles with Controlled Configuration. *J. Phys. Chem. C* **2012**, *116*, 2500–2506. [[CrossRef](#)]
82. Liu, Y.; Wei, S.; Gao, W. Ag/ZnO heterostructures and their photocatalytic activity under visible light: Effect of reducing medium. *J. Hazard. Mater.* **2015**, *287*, 59–68. [[CrossRef](#)] [[PubMed](#)]
83. Subramanian, V.; Wolf, E.; Kamat, P.V. Semiconductor–Metal Composite Nanostructures. To What Extent Do Metal Nanoparticles Improve the Photocatalytic Activity of TiO₂ Films? *J. Phys. Chem. B* **2001**, *105*, 11439–11446. [[CrossRef](#)]
84. Jiang, Z.; Wei, W.; Mao, D.; Chen, C.; Shi, Y.; Lv, X.; Xie, J. Silver-loaded nitrogen-doped yolk-shell mesoporous TiO₂ hollow microspheres with enhanced visible light photocatalytic activity. *Nanoscale* **2015**, *7*, 784–797. [[CrossRef](#)] [[PubMed](#)]
85. Chen, H.; Tu, T.; Wen, M.; Wu, Q. Assembly synthesis of Cu₂O-on-Cu nanowires with visible-light-enhanced photocatalytic activity. *Dalton Trans.* **2015**, *44*, 15645–15652. [[CrossRef](#)] [[PubMed](#)]
86. Li, X.; Sun, Y.; Xiong, T.; Jiang, G.; Zhang, Y.; Wu, Z.; Dong, F. Activation of amorphous bismuth oxide via plasmonic Bi metal for efficient visible-light photocatalysis. *J. Catal.* **2017**, *352*, 102–112. [[CrossRef](#)]
87. Dong, F.; Li, Q.; Sun, Y.; Ho, W.-K. Noble Metal-Like Behavior of Plasmonic Bi Particles as a Cocatalyst Deposited on (BiO)₂CO₃ Microspheres for Efficient Visible Light Photocatalysis. *ACS Catal.* **2014**, *4*, 4341–4350. [[CrossRef](#)]
88. Dong, F.; Zhao, Z.; Sun, Y.; Zhang, Y.; Yan, S.; Wu, Z. An Advanced Semimetal–Organic Bi Spheres–g-C₃N₄ Nanohybrid with SPR-Enhanced Visible-Light Photocatalytic Performance for NO Purification. *Environ. Sci. Technol.* **2015**, *49*, 12432–12440. [[CrossRef](#)] [[PubMed](#)]
89. Gao, Y.; Huang, Y.; Li, Y.; Zhang, Q.; Cao, J.-j.; Ho, W.; Lee, S.C. Plasmonic Bi/ZnWO₄ Microspheres with Improved Photocatalytic Activity on NO Removal under Visible Light. *ACS Sustain. Chem. Eng.* **2016**, *4*, 6912–6920. [[CrossRef](#)]
90. Dong, F.; Xiong, T.; Yan, S.; Wang, H.; Sun, Y.; Zhang, Y.; Huang, H.; Wu, Z. Facets and defects cooperatively promote visible light plasmonic photocatalysis with Bi nanowires@BiOCl nanosheets. *J. Catal.* **2016**, *344*, 401–410. [[CrossRef](#)]
91. Zhang, N.; Liu, S.; Fu, X.; Xu, Y.-J. Synthesis of M@TiO₂ (M = Au, Pd, Pt) Core–Shell Nanocomposites with Tunable Photoreactivity. *J. Phys. Chem. C* **2011**, *115*, 9136–9145. [[CrossRef](#)]
92. Cushing, S.K.; Li, J.; Meng, F.; Senty, T.R.; Suri, S.; Zhi, M.; Li, M.; Bristow, A.D.; Wu, N. Photocatalytic Activity Enhanced by Plasmonic Resonant Energy Transfer from Metal to Semiconductor. *J. Am. Chem. Soc.* **2012**, *134*, 15033–15041. [[CrossRef](#)] [[PubMed](#)]
93. Kong, L.; Chen, W.; Ma, D.; Yang, Y.; Liu, S.; Huang, S. Size control of Au@Cu₂O octahedra for excellent photocatalytic performance. *J. Mater. Chem.* **2012**, *22*, 719–724. [[CrossRef](#)]
94. Yang, T.-T.; Chen, W.-T.; Hsu, Y.-J.; Wei, K.-H.; Lin, T.-Y.; Lin, T.-W. Interfacial Charge Carrier Dynamics in Core-Shell Au-CdS Nanocrystals. *J. Phys. Chem. C* **2010**, *114*, 11414–11420. [[CrossRef](#)]
95. Wu, X.-F.; Song, H.-Y.; Yoon, J.-M.; Yu, Y.-T.; Chen, Y.-F. Synthesis of Core-Shell Au@TiO₂ Nanoparticles with Truncated Wedge-Shaped Morphology and Their Photocatalytic Properties. *Langmuir* **2009**, *25*, 6438–6447. [[CrossRef](#)] [[PubMed](#)]

96. Chen, M.; Li, Y.; Wang, Z.; Gao, Y.; Huang, Y.; Cao, J.; Ho, W.; Lee, S. Controllable Synthesis of Core–Shell Bi@Amorphous Bi₂O₃ Nanospheres with Tunable Optical and Photocatalytic Activity for NO Removal. *Ind. Eng. Chem. Res.* **2017**, *56*, 10251–10258. [[CrossRef](#)]
97. Li, J.T.; Cushing, S.K.; Bright, J.; Meng, F.K.; Senty, T.R.; Zheng, P.; Bristow, A.D.; Wu, N.Q. Ag@Cu₂O Core-Shell Nanoparticles as Visible-Light Plasmonic Photocatalysts. *ACS Catal.* **2013**, *3*, 47–51. [[CrossRef](#)]
98. Li, Q.; Wang, F.; Sun, L.; Jiang, Z.; Ye, T.; Chen, M.; Bai, Q.; Wang, C.; Han, X. Design and Synthesis of Cu@CuS Yolk–Shell Structures with Enhanced Photocatalytic Activity. *Nano-Micro Lett.* **2017**, *9*, 35. [[CrossRef](#)] [[PubMed](#)]
99. Li, P.; Wei, Z.; Wu, T.; Peng, Q.; Li, Y. Au–ZnO Hybrid Nanopyramids and Their Photocatalytic Properties. *J. Am. Chem. Soc.* **2011**, *133*, 5660–5663. [[CrossRef](#)] [[PubMed](#)]
100. Yao, K.X.; Liu, X.; Zhao, L.; Zeng, H.C.; Han, Y. Site-specific growth of Au particles on ZnO nanopyramids under ultraviolet illumination. *Nanoscale* **2011**, *3*, 4195–4200. [[CrossRef](#)] [[PubMed](#)]
101. Muñoz-Batista, M.J.; Ballari, M.M.; Kubacka, A.; Alfano, O.M.; Fernández-García, M. Braiding kinetics and spectroscopy in photo-catalysis: The spectro-kinetic approach. *Chem. Soc. Rev.* **2019**, *48*, 637–682. [[CrossRef](#)] [[PubMed](#)]
102. Davies, M.J. Detection and characterisation of radicals using electron paramagnetic resonance (EPR) spin trapping and related methods. *Methods* **2016**, *109*, 21–30. [[CrossRef](#)] [[PubMed](#)]
103. Shiraiishi, Y.; Hirai, T. Selective organic transformations on titanium oxide-based photocatalysts. *J. Photochem. Photobiol. C Photochem. Rev.* **2008**, *9*, 157–170. [[CrossRef](#)]
104. Lang, X.; Chen, X.; Zhao, J. Heterogeneous visible light photocatalysis for selective organic transformations. *Chem. Soc. Rev.* **2014**, *43*, 473–486. [[CrossRef](#)] [[PubMed](#)]
105. Kisch, H. Semiconductor photocatalysis for organic synthesis. *Adv. Photochem.* **2001**, *26*, 93–143.
106. Park, H.; Choi, W. Photocatalytic conversion of benzene to phenol using modified TiO₂ and polyoxometalates. *Catal. Today* **2005**, *101*, 291–297. [[CrossRef](#)]
107. Ide, Y.; Nakamura, N.; Hattori, H.; Ogino, R.; Ogawa, M.; Sadakane, M.; Sano, T. Sunlight-induced efficient and selective photocatalytic benzene oxidation on TiO₂-supported gold nanoparticles under CO₂ atmosphere. *Chem. Commun.* **2011**, *47*, 11531–11533. [[CrossRef](#)] [[PubMed](#)]
108. Yuzawa, H.; Kumagai, J.; Yoshida, H. Reaction Mechanism of Aromatic Ring Amination of Benzene and Substituted Benzenes by Aqueous Ammonia over Platinum-Loaded Titanium Oxide Photocatalyst. *J. Phys. Chem. C* **2013**, *117*, 11047–11058. [[CrossRef](#)]
109. Yuzawa, H.; Yoshida, H. Direct aromatic-ring amination by aqueous ammonia with a platinum loaded titanium oxide photocatalyst. *Chem. Commun.* **2010**, *46*, 8854–8856. [[CrossRef](#)] [[PubMed](#)]
110. Tanaka, A.; Hashimoto, K.; Kominami, H. Preparation of Au/CeO₂ Exhibiting Strong Surface Plasmon Resonance Effective for Selective or Chemoselective Oxidation of Alcohols to Aldehydes or Ketones in Aqueous Suspensions under Irradiation by Green Light. *J. Am. Chem. Soc.* **2012**, *134*, 14526–14533. [[CrossRef](#)] [[PubMed](#)]
111. Zhang, N.; Fu, X.; Xu, Y.-J. A facile and green approach to synthesize Pt@CeO₂ nanocomposite with tunable core-shell and yolk-shell structure and its application as a visible light photocatalyst. *J. Mater. Chem.* **2011**, *21*, 8152–8158. [[CrossRef](#)]
112. Pradhan, S.; Ghosh, D.; Chen, S. Janus Nanostructures Based on Au–TiO₂ Heterodimers and Their Photocatalytic Activity in the Oxidation of Methanol. *ACS Appl. Mater. Interfaces* **2009**, *1*, 2060–2065. [[CrossRef](#)] [[PubMed](#)]
113. Tada, H.; Ishida, T.; Takao, A.; Ito, S. Drastic Enhancement of TiO₂-Photocatalyzed Reduction of Nitrobenzene by Loading Ag Clusters. *Langmuir* **2004**, *20*, 7898–7900. [[CrossRef](#)] [[PubMed](#)]
114. Xie, S.; Wang, Y.; Zhang, Q.; Deng, W.; Wang, Y. MgO- and Pt-Promoted TiO₂ as an Efficient Photocatalyst for the Preferential Reduction of Carbon Dioxide in the Presence of Water. *ACS Catal.* **2014**, *4*, 3644–3653. [[CrossRef](#)]
115. Zhai, Q.; Xie, S.; Fan, W.; Zhang, Q.; Wang, Y.; Deng, W.; Wang, Y. Photocatalytic Conversion of Carbon Dioxide with Water into Methane: Platinum and Copper(I) Oxide Co-catalysts with a Core-Shell Structure. *Angew. Chem. Int. Ed.* **2013**, *52*, 5776–5779. [[CrossRef](#)] [[PubMed](#)]
116. Liu, L.; Pitts, D.T.; Zhao, H.; Zhao, C.; Li, Y. Silver-incorporated bicrystalline (anatase/brookite) TiO₂ microspheres for CO₂ photoreduction with water in the presence of methanol. *Appl. Catal. A Gen.* **2013**, *467*, 474–482. [[CrossRef](#)]

117. Wang, Z.; Teramura, K.; Hosokawa, S.; Tanaka, T. Photocatalytic conversion of CO₂ in water over Ag-modified La₂Ti₂O₇. *Appl. Catal. B Environ.* **2015**, *163*, 241–247. [[CrossRef](#)]
118. Feng, X.; Sloppy, J.D.; LaTemp, T.J.; Paulose, M.; Komarneni, S.; Bao, N.; Grimes, C.A. Synthesis and deposition of ultrafine Pt nanoparticles within high aspect ratio TiO₂ nanotube arrays: Application to the photocatalytic reduction of carbon dioxide. *J. Mater. Chem.* **2011**, *21*, 13429–13433. [[CrossRef](#)]
119. Sarina, S.; Zhu, H.; Jaatinen, E.; Xiao, Q.; Liu, H.; Jia, J.; Chen, C.; Zhao, J. Enhancing Catalytic Performance of Palladium in Gold and Palladium Alloy Nanoparticles for Organic Synthesis Reactions through Visible Light Irradiation at Ambient Temperatures. *J. Am. Chem. Soc.* **2013**, *135*, 5793–5801. [[CrossRef](#)] [[PubMed](#)]
120. Jiao, Z.; Zhai, Z.; Guo, X.; Guo, X.-Y. Visible-Light-Driven Photocatalytic Suzuki–Miyaura Coupling Reaction on Mott–Schottky-type Pd/SiC Catalyst. *J. Phys. Chem. C* **2015**, *119*, 3238–3243. [[CrossRef](#)]
121. Kudo, A.; Miseki, Y. Heterogeneous photocatalyst materials for water splitting. *Chem. Soc. Rev.* **2009**, *38*, 253–278. [[CrossRef](#)] [[PubMed](#)]
122. Maeda, K.; Domen, K. Photocatalytic Water Splitting: Recent Progress and Future Challenges. *J. Phys. Chem. Lett.* **2010**, *1*, 2655–2661. [[CrossRef](#)]
123. Ahmad, H.; Kamarudin, S.K.; Minggu, L.J.; Kassim, M. Hydrogen from photo-catalytic water splitting process: A review. *Renew. Sustain. Energy Rev.* **2015**, *43*, 599–610. [[CrossRef](#)]
124. Bi, L.; Gao, X.; Ma, Z.; Zhang, L.; Wang, D.; Xie, T. Enhanced Separation Efficiency of PtNi_x/g-C₃N₄ for Photocatalytic Hydrogen Production. *ChemCatChem* **2017**, *9*, 3779–3785. [[CrossRef](#)]
125. Ingram, D.B.; Linic, S. Water Splitting on Composite Plasmonic-Metal/Semiconductor Photoelectrodes: Evidence for Selective Plasmon-Induced Formation of Charge Carriers near the Semiconductor Surface. *J. Am. Chem. Soc.* **2011**, *133*, 5202–5205. [[CrossRef](#)] [[PubMed](#)]
126. Munoz-Batista, M.J.; Meira, D.M.; Colon, G.; Kubacka, A.; Fernandez-Garcia, M. Phase-Contact Engineering in Mono- and Bimetallic Cu-Ni Co-catalysts for Hydrogen Photocatalytic Materials. *Angew. Chem. -Int. Ed.* **2018**, *57*, 1199–1203. [[CrossRef](#)] [[PubMed](#)]
127. Hu, Z.; Yu, J.C. Pt₃Co-loaded CdS and TiO₂ for photocatalytic hydrogen evolution from water. *J. Mater. Chem. A* **2013**, *1*, 12221–12228. [[CrossRef](#)]
128. Zhang, X.; Liu, Y.; Kang, Z. 3D Branched ZnO Nanowire Arrays Decorated with Plasmonic Au Nanoparticles for High-Performance Photoelectrochemical Water Splitting. *ACS Appl. Mater. Interfaces* **2014**, *6*, 4480–4489. [[CrossRef](#)] [[PubMed](#)]
129. Yin, Z.; Chen, B.; Bosman, M.; Cao, X.; Chen, J.; Zheng, B.; Zhang, H. Au Nanoparticle-Modified MoS₂ Nanosheet-Based Photoelectrochemical Cells for Water Splitting. *Small* **2014**, *10*, 3537–3543. [[CrossRef](#)] [[PubMed](#)]
130. Zhang, C.; Shao, M.; Ning, F.; Xu, S.; Li, Z.; Wei, M.; Evans, D.G.; Duan, X. Au nanoparticles sensitized ZnO nanorod@nanoplatelet core-shell arrays for enhanced photoelectrochemical water splitting. *Nano Energy* **2015**, *12*, 231–239. [[CrossRef](#)]
131. Sheeney-Haj-Ichia, L.; Pogorelova, S.; Gofer, Y.; Willner, I. Enhanced Photoelectrochemistry in CdS/Au Nanoparticle Bilayers. *Adv. Funct. Mater.* **2004**, *14*, 416–424. [[CrossRef](#)]
132. Zhukovskiy, M.; Tongying, P.; Yashan, H.; Wang, Y.; Kuno, M. Efficient Photocatalytic Hydrogen Generation from Ni Nanoparticle Decorated CdS Nanosheets. *ACS Catal.* **2015**, *5*, 6615–6623. [[CrossRef](#)]
133. Rosseler, O.; Shankar, M.V.; Du, M.K.-L.; Schmidlin, L.; Keller, N.; Keller, V. Solar light photocatalytic hydrogen production from water over Pt and Au/TiO₂(anatase/rutile) photocatalysts: Influence of noble metal and porogen promotion. *J. Catal.* **2010**, *269*, 179–190. [[CrossRef](#)]
134. Gu, Q.; Long, J.; Fan, L.; Chen, L.; Zhao, L.; Lin, H.; Wang, X. Single-site Sn-grafted Ru/TiO₂ photocatalysts for biomass reforming: Synergistic effect of dual co-catalysts and molecular mechanism. *J. Catal.* **2013**, *303*, 141–155. [[CrossRef](#)]
135. Hong, J.W.; Wi, D.H.; Lee, S.-U.; Han, S.W. Metal–Semiconductor Heteronanocrystals with Desired Configurations for Plasmonic Photocatalysis. *J. Am. Chem. Soc.* **2016**, *138*, 15766–15773. [[CrossRef](#)] [[PubMed](#)]
136. Ma, X.; Zhao, K.; Tang, H.; Chen, Y.; Lu, C.; Liu, W.; Gao, Y.; Zhao, H.; Tang, Z. New Insight into the Role of Gold Nanoparticles in Au@CdS Core–Shell Nanostructures for Hydrogen Evolution. *Small* **2014**, *10*, 4664–4670. [[CrossRef](#)] [[PubMed](#)]

137. Ngaw, C.K.; Xu, Q.; Tan, T.T.Y.; Hu, P.; Cao, S.; Loo, J.S.C. A strategy for in-situ synthesis of well-defined core-shell Au@TiO₂ hollow spheres for enhanced photocatalytic hydrogen evolution. *Chem. Eng. J.* **2014**, *257*, 112–121. [[CrossRef](#)]
138. Lee, Y.J.; Joo, J.B.; Yin, Y.; Zaera, F. Evaluation of the Effective Photoexcitation Distances in the Photocatalytic Production of H₂ from Water using Au@Void@TiO₂ Yolk-Shell Nanostructures. *ACS Energy Lett.* **2016**, *1*, 52–56. [[CrossRef](#)]
139. Yu, Z.B.; Xie, Y.P.; Liu, G.; Lu, G.Q.; Ma, X.L.; Cheng, H.-M. Self-assembled CdS/Au/ZnO heterostructure induced by surface polar charges for efficient photocatalytic hydrogen evolution. *J. Mater. Chem. A* **2013**, *1*, 2773–2776. [[CrossRef](#)]
140. Chava, R.K.; Do, J.Y.; Kang, M. Smart Hybridization of Au Coupled CdS Nanorods with Few Layered MoS₂ Nanosheets for High Performance Photocatalytic Hydrogen Evolution Reaction. *ACS Sustain. Chem. Eng.* **2018**, *6*, 6445–6457. [[CrossRef](#)]
141. Kim, Y.G.; Jo, W.-K. Photodeposited-metal/CdS/ZnO heterostructures for solar photocatalytic hydrogen production under different conditions. *Int. J. Hydrogen Energy* **2017**, *42*, 11356–11363. [[CrossRef](#)]
142. Zhou, H.; Pan, J.; Ding, L.; Tang, Y.; Ding, J.; Guo, Q.; Fan, T.; Zhang, D. Biomass-derived hierarchical porous CdS/M/TiO₂ (M = Au, Ag, Pt, Pd) ternary heterojunctions for photocatalytic hydrogen evolution. *Int. J. Hydrogen Energy* **2014**, *39*, 16293–16301. [[CrossRef](#)]
143. Wang, Q.; Hisatomi, T.; Ma, S.S.K.; Li, Y.; Domen, K. Core/Shell Structured La- and Rh-Codoped SrTiO₃ as a Hydrogen Evolution Photocatalyst in Z-Scheme Overall Water Splitting under Visible Light Irradiation. *Chem. Mater.* **2014**, *26*, 4144–4150. [[CrossRef](#)]
144. Maeda, K.; Teramura, K.; Lu, D.; Saito, N.; Inoue, Y.; Domen, K. Noble-metal/Cr₂O₃ core/shell nanoparticles as a cocatalyst for photocatalytic overall water splitting. *Angew. Chem. Int. Ed.* **2006**, *45*, 7806–7809. [[CrossRef](#)] [[PubMed](#)]
145. Matsunaga, T.; Tomoda, R.; Nakajima, T.; Wake, H. Photoelectrochemical sterilization of microbial cells by semiconductor powders. *FEMS Microbiol. Lett.* **1985**, *29*, 211–214. [[CrossRef](#)]
146. Gamage, J.; Zhang, Z. Applications of Photocatalytic Disinfection. *Int. J. Photoenergy* **2010**, *2010*, 764870. [[CrossRef](#)]
147. Malato, S.; Fernández-Ibañez, P.; Maldonado, M.I.; Blanco, J.; Gernjak, W. Decontamination and disinfection of water by solar photocatalysis: Recent overview and trends. *Catal. Today* **2009**, *147*, 1–59. [[CrossRef](#)]
148. Byrne, J.A.; Fernandez-Ibañez, P.A.; Dunlop, P.S.M.; Alrousan, D.M.A.; Hamilton, J.W.J. Photocatalytic Enhancement for Solar Disinfection of Water: A Review. *Int. J. Photoenergy* **2011**, *2011*, 798051. [[CrossRef](#)]
149. Sarria, V.; Parra, S.; Adler, N.; Péringer, P.; Benitez, N.; Pulgarin, C. Recent developments in the coupling of photoassisted and aerobic biological processes for the treatment of biorecalcitrant compounds. *Catal. Today* **2002**, *76*, 301–315. [[CrossRef](#)]
150. Dalrymple, O.K.; Stefanakos, E.; Trotz, M.A.; Goswami, D.Y. A review of the mechanisms and modeling of photocatalytic disinfection. *Appl. Catal. B Environ.* **2010**, *98*, 27–38. [[CrossRef](#)]
151. Muñoz-Batista, M.J.; Fontelles-Carceller, O.; Ferrer, M.; Fernández-García, M.; Kubacka, A. Disinfection capability of Ag/g-C₃N₄ composite photocatalysts under UV and visible light illumination. *Appl. Catal. B Environ.* **2016**, *183*, 86–95. [[CrossRef](#)]
152. Pratap Reddy, M.; Venugopal, A.; Subrahmanyam, M. Hydroxyapatite-supported Ag-TiO₂ as Escherichia coli disinfection photocatalyst. *Water Res.* **2007**, *41*, 379–386. [[CrossRef](#)] [[PubMed](#)]
153. Kumar, R.V.; Raza, G. Photocatalytic disinfection of water with Ag-TiO₂ nanocrystalline composite. *Ionics* **2009**, *15*, 579–587. [[CrossRef](#)]
154. Liu, L.; Liu, Z.; Bai, H.; Sun, D.D. Concurrent filtration and solar photocatalytic disinfection/degradation using high-performance Ag/TiO₂ nanofiber membrane. *Water Res.* **2012**, *46*, 1101–1112. [[CrossRef](#)] [[PubMed](#)]
155. Rtimi, S.; Giannakis, S.; Sanjines, R.; Pulgarin, C.; Bensimon, M.; Kiwi, J. Insight on the photocatalytic bacterial inactivation by co-sputtered TiO₂-Cu in aerobic and anaerobic conditions. *Appl. Catal. B Environ.* **2016**, *182*, 277–285. [[CrossRef](#)]
156. Zhu, L.; He, C.; Huang, Y.; Chen, Z.; Xia, D.; Su, M.; Xiong, Y.; Li, S.; Shu, D. Enhanced photocatalytic disinfection of E. coli 8099 using Ag/BiOI composite under visible light irradiation. *Sep. Purif. Technol.* **2012**, *91*, 59–66. [[CrossRef](#)]

157. Shi, H.; Li, G.; Sun, H.; An, T.; Zhao, H.; Wong, P.-K. Visible-light-driven photocatalytic inactivation of *E. coli* by Ag/AgX-CNTs (X=Cl, Br, I) plasmonic photocatalysts: Bacterial performance and deactivation mechanism. *Appl. Catal. B Environ.* **2014**, *158–159*, 301–307. [[CrossRef](#)]
158. Gao, P.; Ng, K.; Sun, D.D. Sulfonated graphene oxide–ZnO–Ag photocatalyst for fast photodegradation and disinfection under visible light. *J. Hazard. Mater.* **2013**, *262*, 826–835. [[CrossRef](#)] [[PubMed](#)]
159. Das, S.; Sinha, S.; Suar, M.; Yun, S.-I.; Mishra, A.; Tripathy, S.K. Solar-photocatalytic disinfection of *Vibrio cholerae* by using Ag@ZnO core–shell structure nanocomposites. *J. Photochem. Photobiol. B Biol.* **2015**, *142*, 68–76. [[CrossRef](#)] [[PubMed](#)]



© 2019 by the authors. Licensee MDPI, Basel, Switzerland. This article is an open access article distributed under the terms and conditions of the Creative Commons Attribution (CC BY) license (<http://creativecommons.org/licenses/by/4.0/>).